Université de Montréal

Dynamic magnetic resonance spectroscopy of phosphate energetics during muscle exercise and recovery

par
Bahare Sabouri

Département Institut de Génie Biomédical, Université de Montréal
Faculté des arts et des sciences

Mémoire présenté à la Faculté des études supérieures
en vue de l'obtention du grade de Maître ès sciences (M.Sc.)
en Génie Biomédical

December, 2014

Université de Montréal
Faculté des études supérieures

Ce mémoire intitulé:

Dynamic magnetic resonance spectroscopy of phosphate energetics during muscle exercise and recovery

présenté par:

Bahare Sabouri

a été évalué par un jury composé des personnes suivantes:

Gilles Beaudoin,	président-rapporteur
Richard Hoge,	directeur de recherche
Hélène Girouard,	membre du jury

Mémoire accepté le: . . . . . .

RÉSUMÉ

L'importance des échanges de phosphore liés à l'apparition de troubles et de maladies neurodégénèratives a suscité l'intérêt des chercheurs en ce qui concerne le développement de technologies pouvant détecter ces composés métaboliques. Á l'aide de la spectroscopie en résonance magnétique du phosphore, il est possible de détecter ces métabolites d'une manière non-invasive. Cette technique permet plus particulièrement de mesurer le taux de degénération de la phosphocréatine (PCr) lors de périodes d'exercice et de récupération post-activité.

Cette dernière métrique agit en tant qu'indicateur valide du métabolisme oxydatif mitochondrial dans le muscle et permet de différentier un muscle sain d'un muscle pathologique. Pour effectuer l'imagerie ou la spectroscopie par résonance magnétique, de nombreux outils cliniques peuvent être utilisés afin de générer des images comprenant une variété de contrastes anatomiques et fonctionnels. Par contre, ces contrastes ne peuvent être habituellement produits qu'à partir des molécules d'eau ou des atomes d'hydrogène renfermés dans les tissus biologiques et les outils permettant de générer les images correspondantes demeurent, pour la plupart, insensibles à la présence d'autres atomes d'intérêt.

Au cours de ce projet, il a été question d'obtenir un spectre du phosphore à partir de l'activité musculaire chez l'humain *in vivo* en se servant de la technique de spectroscopie de type ^{31}P. Pour ce faire, une antenne radiofréquence à deux canaux, devant être syntonisée à la fréquence de résonance du phosphore, a d'abord été conçue et fabriquée en laboratoire pour ensuite être validée lors d'expériences sur une plateforme IRM 3T de marque Siemens. Les spectres du phosphore furent acquis sur un fantôme, une solution de phosphate de potassium à une concentration de 100 mM, ainsi que sur le mollet d'un sujet humain au cours d'une période de repos, d'exercice et de récupération. Le spectre obtenu à la suite de cette dernière expérience démontre la présence accrue du phosphore lors de procédés métaboliques à haute teneur énergétique impliquant la dégradation de phosphates. Par la suite, il a été question d'observer la variation des niveaux de PCr durant des périodes d'exercice et de récupération chez 5 jeunes adultes effectuant une série

de flexions plantaires ayant un élément résistif attaché à leurs pieds.

La démarche entreprise au cours de ce projet permettra l'utilisation future des techniques quantitatives en spectroscopie pour l'évaluation du métabolisme des phosphates chez des patients souffrant de maladies coronariennes ainsi que chez des sujets contrôles sains provenant du même ensemble démographique.

Mots-clés : *In vivo*, Spectroscopie, Antenne radiofréquence de surface, IRM

ABSTRACT

Entailing of phosphorus exchanges in most bio-chemicals as a key factor in disease, increases researcher's interest to develop the technologies capable of detecting this metabolite. Phosphorus magnetic resonance spectroscopy is able to detect key metabolites in a non-invasive manner. Particularly, it offers the ability to measure the dynamic rate of phosphocreatine(PCr) degeneration through the exercise and recovery. This metric as a valid indication of mitochondrial oxidative metabolism in muscle, differentiate between normal and pathological state.

To do magnetic resonance imaging and spectroscopy, clinical research tools provide a wide variety of anatomical and functional contrasts, however they are typically restricted to the tissues containing water or hydrogen atoms and they are still blind to the biochemicals of other atoms of interests.

Through this project we intended to obtain the phosphorus spectrum in human body – specificadeneratively in muscle – using ^{31}P spectroscopy. To do so a double loop RF surface coil, tuned to phosphorus frequency, is designed and fabricated using bench work facilities and then validated through *in vitro* spectroscopy using 3 Tesla Siemens scanner.

We acquired *in vitro* as well as *in vivo* phosphorus spectrum in a 100 mM potassium phosphate phantom and human calf muscle in rest-exercise-recovery phase in a 3T MR scanner. The spectrum demonstrates the main constituent in high-energy phosphate metabolism. We also observed the dynamic variation of PCr for five young healthy subjects who performed planter flexions using resistance band during exercise and recovery.

The took steps in this project pave the way for future application of spectroscopic quantification of phosphate metabolism in patients affected by carotid artery disease as well as in age-matched control subjects.

Keywords: Dynamic, *In vivo*, Spectroscopy, RF surface coil, MRI.

CONTENTS

LIST OF TABLES

LIST OF FIGURES

LIST OF APPENDICES

LIST OF ABBREVIATIONS

AD	Alzheimer's Disease
ATP	Adenosine Tri Phosphate
ADP	Adenosine Di Phosphate
FID	Free induction decay
mM	milli-Molar
MRI	Magnetic Resonance Imaging
MRS	Magnetic Resonance Spectroscopy
NF	Noise factor
NMR	Nuclear Magnetic Resonance
PCr	Phosphocreatine
Pi	Inorganic Phosphate
RF	Radio Frequency
ROI	Region Of Interest
SNR	Signal to Noise Ratio
SAR	Specific Absorption Rate
T1	Longitudinal relaxation time
T2	Transverse relaxation time
TE	Time for Echo
TR	Repetition Time

NOTATION

γ	Gyro magnetic ratio
ν	Larmour frequency
M	Magnetization vector
i, j	$\sqrt{-1}$
σ	Shielding factor
δ	Chemical shift
B	Magnetic field
λ	Wave length

To Pooran and Sepideh for all their supports

ACKNOWLEDGMENTS

I would like to thank our funding agencies, CFI and CIHR that have provided the resources necessary to fund this project. This project is above all a collaboration between the LINeV laboratory and the CHUM who made possible a research agreement with Siemens.

I wish to thank my principal supervisor Rick Hoge for all his support and encouragement throughout the project. An special thanks goes to Gilles Beaudoin from CHUM. His advice greatly contributed to this project.

Thanks to Raphaël Paquin, from Siemens and Jamie Near, from CIC at Douglas Institute for their consultation.

To my friends and colleagues from LINeV, Isabelle Lajoie, Anne-Marie Bédard, Scott Nugent, Marius Tuznik, Lucile Sink and Kenneth Dyson. Thank you for all the great and the not so good moments and your companionship during the long days. You are an incredible resource that I will greatly miss.

To the UNF that have trained me, Carollyn Hurst and André Cyr, thank you for your help, discussions and spending so much time with me.

And of course, I would like to thank the most important people in my life, my mother Pooran and my sister Sepideh, I couldn't be here without your help. Thank you for all of your sacrifices and your unwavering support.

PREFACE

There is a growing demand for non-invasive techniques to assess the tissue metabolism and function. Such techniques propose alternatives for determining tissue properties in the normal state and changes in the disease state [3]. Among human diseases affecting skeletal muscle; the prevalence of type 2 diabetes in the youth and pressure sore among the elderly is increasing rapidly. The development of technologies to diagnose such disorders will greatly contribute to the management of their prevalence [4].

Among all the image modalities, positron emission tomography (PET) and magnetic resonance spectroscopy (MRS) are the gold standards when it comes to measuring metabolism [5]. However, MRS offers the non-invasive alternative that is free of the radiation, [6]. Most scanners used in hospitals and research centers are tuned to image protons. In contrast, tissue metabolism is based on the exchange of phosphorus metabolism [7].

This project mainly concerns spectroscopic quantification of phosphocreatine metabolism in the muscle of healthy young subjects [8]. Most ^{31}P NMR studies are conducted in human muscle due to the high concentrations of phosphorus in this area [9].

The main objective of this project concerns the dynamic measurement of phosphocreatine in human skeletal muscle when the calf muscle goes through exercise and recovery period. To achieve this goal we chose nuclear magnetic resonance spectroscopy technique, particularly ^{31}P NMR. We are aiming to reach a level of sensitivity in the spectrum that accurately projects the phosphocreatine depletion and replenishment. Other than that, the resting state spectrum should clearly demonstrate the main constituent of the phosphorus spectrum –including PCr, ATPs and inorganic phosphate–of the skeletal muscle. Various techniques and hardware were developed for phosphorus imaging on 3 Tesla MRI scanner. In the first phase of the project we develop efficient analysis tools to acquire and quantify phosphorus components. The next step was to optimize the hardware, which is essential for accurate quantification. Finally, the optimized hardware was used to probe the role of phosphorus in biological components, such as adenosine triphosphate (ATP) and phosphocreatine (PCr) in healthy subjects undergoing a func-

tional task.

Hardware aspects of the project included the development of an RF coil. Tests of the hardware were achieved using a double loop coil tuned to the phosphorus resonate frequency on phantoms containing various concentrations of inorganic phosphate. Then the hardware was used to run the experiments on the calf muscle of human subjects. It has been shown through the experiments that the acquired signal in this area gives a robust signal of PCr during contraction exercise and recovery.

Our lab is well experienced in quantitative neuroimaging. Phosphorus spectroscopy is used for the study of phosphorus components in cardiac ischemia and mitochondrial dysfunction in Alzheimer's disease [10]. The early stage of Alzheimer's disease (AD) demonstrates a metabolic alteration [7], [11]. Measurement and monitoring of these alterations are a growing interest among researchers. They have an essential role in the understanding and prevention of mild cognitive impairment (MCI) and the progression to AD [12]. Diagnostics using traditional magnetic resonance imaging (MRI) involves various challenges. Proton magnetic resonance spectroscopy ^{1}H NMR can help to identify hydrogenated components of interest. However, this method is still blind to most bio-chemicals involved in phosphorus exchanges of oxidative metabolism.

In the future, the RF coil will be modified to be applicable for use on the brain. Phosphorus metabolism changes will be observed in the healthy brain while doing a functional task. This project has high potential to provide valuable quantitative information about energy metabolism which helps the understanding of pathophysiology in neurodegenerative diseases.

CHAPTER 1

INTRODUCTION

Molecular medicine has benefited profoundly from nuclear magnetic resonance (NMR) spectroscopy. The development of high field strength magnets and increased accessibility to whole-body scanners for magnetic resonance (MR) imaging initiated the motivation to use non-proton spectroscopy as a diagnostic tool. Among common nuclei with NMR capability, ^{31}P and ^{13}C are of particular interest. ^{13}C exists in organic compounds and is extensively associated with topics such as glucose labeling. ^{31}P comprises 100% of phosphorus content in the human body and plays a key role in ischemic cardiac myopathy diagnosis [13], [14], various brain diseases [15] and in the examination of cancer treatment effectiveness [16], [17]. Among the phosphorus metabolites, adenosine triphosphate (ATP) and phosphocreatine (PCr) are responsible for the regulation of cellular energy delivery and responding to changes in muscular tissue energy demand [18]. Recent advances in spectroscopy techniques and equipment have paved the way for the *in vivo* study of animal and human biological samples.

1.1 Magnetic resonance (MR) physics

NMR is based on the principals of nuclei spins subjected to a strong static magnetic field and their reaction based on their chemical environment [19]. Specificities concerning the physics of spins is a complicated topic, which is not the concern of this thesis. To understand the concept of NMR we first have to acknowledge the nuclear behavior of the spins within a magnetic field. This can be presented as two main perspectives: classical and quantum.

1.1.1 Classical description

The proton can be seen as a rotating object with an electrical charge that is placed in a magnetic field. This will result in the generation of an angular and magnetic mo-

ment. Conceptually, momentum is the tendency for a proton to continue its motion indefinitely. The relationship between magnetic and angular moment is a nuclear specific constant that makes two quantities equal Eq. 1.1 (γ is the gyro magnetic ratio). Hydrogen is the simplest molecule with one positive charge, referred to as a proton. The magnetic moment is as small as $1.4102 \times 10^{-26}\ JT^{-1}$ and the gyro magnetic ratio is $\frac{\gamma}{2\pi} = 42.575\ \frac{MHz}{T}$

$$\mu = \gamma L \tag{1.1}$$

Where μ is the magnetic moment and L is the angular moment.
In the absence of an external magnetic field, protons align randomly. When they are subjected to a static magnetic field, B_0, protons will start to precess about B_0 and are influenced by a torque given by Eq. 1.2. Torque causes the angular moment changes as Eq. 1.3.

$$T = \mu B_0 \tag{1.2}$$

$$T = \frac{dL}{dt} \tag{1.3}$$

Combining all the former equations gives

$$\frac{d\mu}{dt} = \gamma \mu B_0 \tag{1.4}$$

Alternatively the rotation of μ around B_0 can be expressed as:

$$\frac{d\mu}{dt} = \mu \omega_0 \tag{1.5}$$

Combining Eq. 1.4 and Eq. 1.5 gives the Larmor equation and Larmor frequency respectively

$$\omega_0 = \mu B_0 \tag{1.6}$$

$$\nu_0 = \frac{\omega_0}{2\pi} = \frac{\gamma}{2\pi} B_0 \tag{1.7}$$

The Larmor frequency is proportional to the strength of B_0 as well as gyro magnetic ratio – the characteristic of the nucleus. On the other hand, once a particle interacts with the magnetic moment in B_0 this results in the magnetic energy, defined byμ:

$$E = -\boldsymbol{\mu} \,.\, \mathbf{B_0} = -\mu \, B_0 \, cos\theta \tag{1.8}$$

θ is the angle between $\mathbf{B_0}$ and the magnetic moment $\boldsymbol{\mu}$. The classical view gives an idea about how magnetic energy relates to the magnetic moment and the static magnetic field. Quantum description in next section provides a picture about the interaction of nuclear spins and electromagnetic waves.

1.1.2 Quantum description

Considering Eq. 1.1, magnetic moment and angular momentums of elementary particles are parallel vectors and they may be given as

$$\mu_z = \gamma(\frac{h}{2\pi})m \tag{1.9}$$

where m depends on the spin quantum number, I, can have $2I+1$ values, $m = I,\ I-1,\ I-2, ... -I$. In an external magnetic field the particle acquires energy given by Eq. 1.8. Considering the quantum description of magnetic and magnetic energy given by the classical view,

$$E = -\mu_z B_0 = -\gamma(\frac{h}{2\pi})mB_0 \tag{1.10}$$

The energy level is quantized due to the discrete value of m and the number of quantized energy level in the magnetic field is 2I+1. This means that once a non-zero spin particle is placed in a magnetic field it can take on one of the $2I+1$ levels of energy, for example for $I = 1/2$ there are two levels of energy ($m = -1/2$ and $1/2$) and the difference between the levels defined as:

$$\Delta E = \gamma(\frac{h}{2\pi})B_0 \tag{1.11}$$

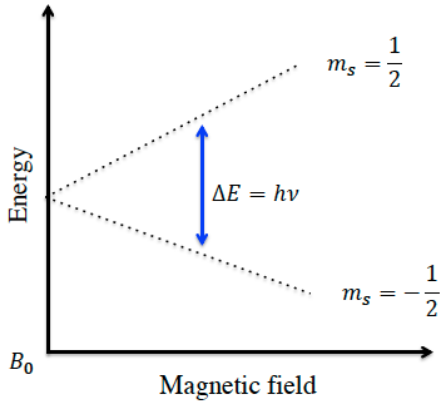

Figure 1.1 – Zeeman splitting; energy level for a nucleus with spin quantum number of 1/2

The resonance phenomena occurs if an oscillating magnetic field is applied perpendicular to μ with a ν_0 frequency. The energy of this magnetic wave is given by Eq. 1.11 and could be rewritten as:

$$\Delta E = h\nu_0 \tag{1.12}$$

Thus the Larmor frequency is given by

$$\nu_0 = (\frac{\gamma}{2\pi})B_0 \tag{1.13}$$

Although Eq. 1.13 and Eq. 1.7 yield the same result, quantum and classic descriptions are two different approaches for understanding the resonance phenomena for NMR.

1.1.3 NMR signal detection

The longitudinal magnetization, M_z has to be dephased from the z axis and tipped to the transverse plane (x-y plane) in order to measure the NMR signal. This requires a

pulsed electromagnetic field, B_1, perpendicular to the main magnetic field B_0 that flips the longitudinal magnetization, M_z, at the resonance frequency ν_0. This consequently increases the transversal magnetization, M_{xy}. A coil perpendicular to B_0 generates the B_1 field, which applies a torque to the nuclear spins and tips $\vec{M}$ by the angle α. This phenomena has been shown on Figure 1.2 on a Bloch sphere and also in a rotating frame when the x-y plane rotates at the Larmor frequency. Normally B_1 is applied through the RF pulses and the strength of the torque depends on the RF pulse duration and the magnetization and M, continues to tip away as long as B_1 exists. In fact the magnetization vector starts processing once it has a nonzero component in the transverse plane. This results in a local magnetic field (B) varying in time. This precessing component is like a small magnet and when it spins inside the loop coil circuit it causes the magnetic flux projected through the loop to vary with time [20].

$$\frac{dM}{dt} \propto \frac{dB}{dt} \tag{1.14}$$

This then induces an EMF as per Faraday's law. The voltage (emf) induced in the detector coil is proportional to the rate of change of the magnetic flux in the coil, which in turn is proportional to the rate of change of the oscillating transverse magnetization. We already learned that Larmor frequency is field dependent, Eq. 1.7 and the nuclei will absorb the most amount of energy at this frequency. With an RF pulse that meets the resonance condition, the magnetization vector tips away from the z axis with a precessional frequency ω_1. Knowing that the magnetic field in the transversal plane is B_1 we will have:

$$\omega_1 = \gamma B_1 \tag{1.15}$$

The receiver coil is sensitive to the transversal magnetization so it detects the most of signal when α is 90 degrees and normally a train of pulses has to be applied to efficiently detect NMR signal.

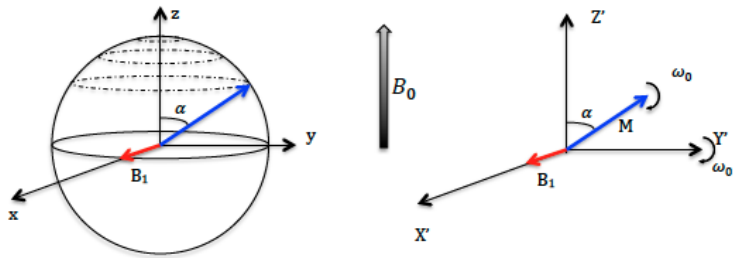

Figure 1.2 – Magnetization M_z is flipped by angle alpha using the field B_1. The left frame describes the motion of the nuclei by a nutation around the z axis. In the right frame of reference the x,y plane is rotating at ω_0 and magnetization, in this example, is seen as tipping along the y' axis.

1.1.4 Bloch equation and bulk magnetization

By tipping the $\overrightarrow{M}$, the resultant vector is broken into two components: M_{xy} transverse and M_z longitudinal magnetization. The longitudinal component returns to its initial state and the transverse component decays; this phenomenon called relaxation. Bloch equation describes the dynamic process which the relaxation occurs. Components of the $\overrightarrow{M}$, including ($M_{x,y}$ and M_z), return to equilibrium through an exponential variation. The transverse relaxation time for $M_{x,y}$ differs from the longitudinal relaxation M_z. The relaxation process of the longitudinal, also called spin-lattice, can be written as:

$$\frac{dM_z}{dt} = \frac{(M_0 - M_z)}{T_1} \tag{1.16}$$

The solution to the differential equation could be written as:

$$M_z = M_0 + (M_z(0) - M_0)e^{-\frac{t}{T_1}} \tag{1.17}$$

T_1 is the longitudinal relaxation, which describes the time that it takes for the longitudinal magnetization to return to equilibrium. During this process the spins energy transfers to the lattice.

The other relaxation, called transverse or spin-spin relaxation, explains the net magnetization decay in the transversal plane from one spin energy level to the other. Equation

for this relaxation is:

$$\frac{(dM_x)}{dt} = -\frac{M_x}{T_2} + \gamma M_y B_0 \tag{1.18}$$

$$\frac{(dM_y)}{dt} = -\frac{M_y}{T_2} + \gamma M_x B_0 \tag{1.19}$$

Solutions for M_x and M_y are:

$$M_x(t) = [M_x(0)cos(\gamma B_0 t) - M_y(0)sin(\gamma B_0 t)]exp^{-t/T2} \tag{1.20}$$

$$My(t) = [-M_x(0)sin(\gamma B_0 t) + M_y(0)cos(\gamma B_0 t)]exp^{-t/T2} \tag{1.21}$$

T_2 is the spin-spin or transverse relaxation time constant. The spins exchange energy between themselves, which results in different rates of spin precession, which decreases the phase coherence. T_1 and T_2 are both time constants that differs from one material to another.

1.1.5 Fourier Transform

The RF pulse is calibrated such that it rotates $\overrightarrow{M}$ by 90 degrees and positions the magnetization in the transverse plane of the rotating frame of reference, Figure 1.2. At this point magnetization precesses about B_0 at the Larmor frequency and induces an electromotive force, emf, in the receiving coil located in the transverse plane. However, transverse magnetization as well as emf decreases in the form of an exponential decay due to T_2 relaxation. The acquired signal in the time domain for a sample is represented as:

$$M_{xy} = M_{xy}(0)e^{-t/T_2} \int e^{i\gamma \Delta B_0(r)t} dr = M_{xy}(0)e^{-t/T_2^*} \tag{1.22}$$

ΔB_0 represents B_0 inhomogeneity and equals equals $(B_0(r) - B_{(0,nom)})$. $B_0(r)$ the magnetic field strength, $B_{(0,nom)}$ the nominal magnetic field strength and M_{xy} is the transverse magnetization. Emf in time domain, called free induction decay, and magnetization in the transversal plane has a complex motion as shown Figure 1.3. The projection vector onto (M_x,t) corresponds to the real portion of $M_{x,y}$, while (M_y,t) corresponds to the imaginary. They describe the complex FID [1].

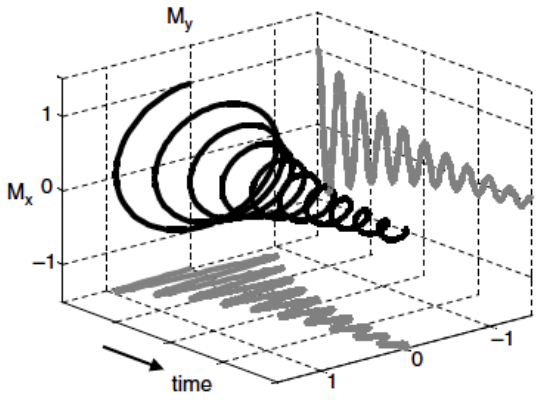

Figure 1.3 – Exponential decay of the magnetization in transversal plane and its relation with Fourier transform, Figure taken from [1]

The NMR signal is a signal in complex domain which includes *x* and *y* components. The time domain data is rarely used in NMR spectroscopy despite the fact that it provides information about the nuclear spins and resonance frequency. The time domain signal may be converted to the frequency domain using a Fourier transformation. A first dimension Fourier transformation of the signal represents the frequency component. The real and imaginary parts of the frequency component represent absorption and dispersion elements –due to the non-zero initial phase of the FID signal. Components of the Lorentzian function are typically used to demonstrate the spectrum.

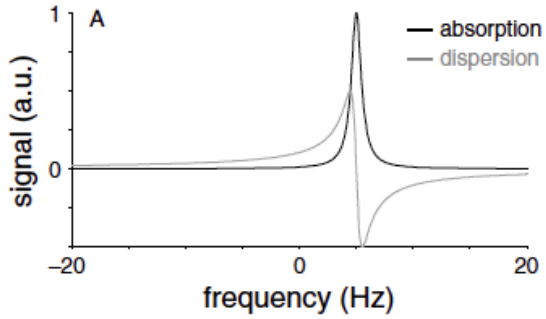

Figure 1.4 – Components of a NMR spectrum; the non-zero initial phase of the FID induces the absorption and dispersion components, Figure taken from [1].

The dispersive component reduces the resolution and in fact the desired mode is the

absorption component. Phase correction of the spectrum eliminates the dispersion part leaving only absorption. Purely absorptive signals have a narrower base that allows us to differentiate peaks which are very close to each other. This differentiation would be much easier if the spectrum has been phase corrected to hold absorptive signals. For the phase correction we simply could manipulate the real and imaginary part as follow:

$$Re(\Delta\phi) = -Im(\Delta\phi = 0)Sin(\phi) + Re(\Delta\phi = 0)cos(\phi) \tag{1.23}$$

$$Im(\Delta\phi) = Re(\Delta\phi = 0)Sin(\phi) + Im(\Delta\phi = 0)cos(\phi) \tag{1.24}$$

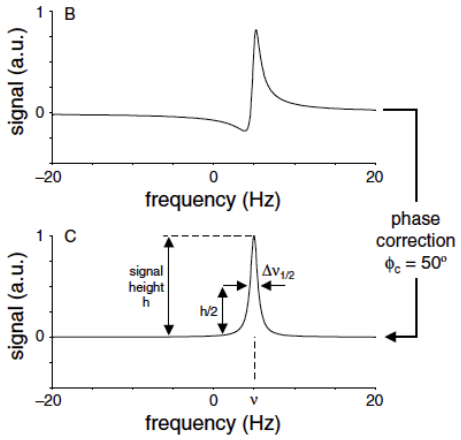

Figure 1.5 – Elimination of dispersion part by phase correction, Figure taken from [1].

1.1.6 Resolution enhancement and SNR improvement

Transverse relaxation time T2 of the spins determines the resolution of the spectra. A long transverse relaxation time leads the spins to decay slowly and fast relaxation provides a quickly decaying FID. The the amount of signal which remains towards the end of the FID determines the resolution. Any data manipulation, e.g. multiplying the FID with a increasing exponential ($e^{t/x}$) will improve the resolution. Conversely, the SNR is determined by the amount of signal at the beginning of the FID. Most manipulations that improve resolution lead to a loss in SNR.

1.1.7 Chemical shift

The signal frequency observed in NMR spectroscopy has a direct relationship to the external magnetic field applied to the nucleus. We saw already the resonance frequency is given by:

$$\nu_0 = (\frac{\gamma}{2\pi})B_0 \tag{1.25}$$

Based on Eq. 1.25, all the nuclear spins have the same resonance frequency as long as they are positioned in the same magnetic field strength. However, it is not true in reality because the resonance frequency is highly sensitive to the chemical environment of the nucleus. The response of the electrons in the nucleus to the external magnetic field produce a microscopic magnetic field, which is able to change the effective magnetic field [21]. Therefore, the real magnetic field influences the nucleus is as follow:

$$B = B_0(1-\delta) \tag{1.26}$$

δ is the shielding factor and for protons is as small as -10^{-5} and for other nuclei may be less than 10^{-3}. It is dimensionless and expressed in parts per million(ppm). Thus, the resonance frequency may be modified as:

$$\nu = (\frac{\gamma}{2\pi})\, B_0\, (1-\delta) \tag{1.27}$$

The chemical shift δ is defined as:

$$\delta = \frac{\nu - \nu_{ref}}{\nu_{ref}} \times 10^6 \tag{1.28}$$

ν and ν_{ref} are the frequency of the compound under investigation and of the reference compound. The reference compound for protons is tetramethylsilane (TMS), which gives zero chemical shift for *in vitro* spectroscopy and phosphocreatine resonance (0.00 ppm) for brain and muscle ^{31}P spectroscopy.

1.1.8 J-coupling

Sometimes the peak in the spectrum splits, this phenomena happens when two or more nuclei interact. The nuclei holding magnetic moments generates a magnetic field. The magnetic field directly influences the neighboring spins. This type of interaction is called bipolar coupling, however, the indirect interaction occurs through the electron cloud of the chemical bond and is called J-coupling or spin-spin coupling. If the spins do not interact with each other then the energy equals $\Delta E = hf$. However during j-coupling of nuclei, the energy will be altered by a coupling constant J and. The possible transition energy could be rewritten as:

$$\Delta E = h(f \pm J/2) \tag{1.29}$$

The result will be a peak split by J Hz on NMR spectrum. Another piece of information that J-coupling provides is the information about the chemical compound, which in *in vivo* spectroscopy it is not of interest since lots of metabolite might be located in the closed position and knowing the chemical and by that J-coupling could decrease the sensitivity of the detection as it decrease the amplitude of the peak or information could be contaminated by other metabolite. Therefore, it is desired to get J-coupling under control or remove it if possible [22].

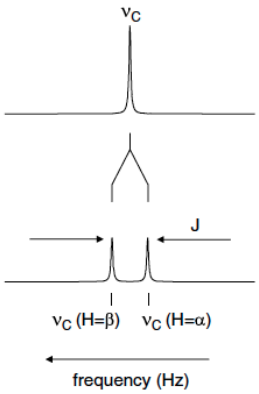

Figure 1.6 – The peak splitting of the ^{1}H due to the J-coupling with ^{13}C, Figure taken from [1].

1.2 Inside the MR

In vivo and *in vitro* spectroscopy uses the MR scanner as it requires a sufficiently strong and highly homogeneous magnetic field. Furthermore, specific sequence for spectroscopic signal acquisition is necessary. Depending on the type of MRS; single voxel spectroscopy, SVS, or chemical shift imaging, CSI, the sequences varies. In SVS, the signal reflects back from a single voxel while in CSI the spectra belongs to the multiple voxels in a projection, on a slice or a volume. Only in the presence of the homogeneous magnetic field a proper analysis – the differences between the metabolite resonance frequencies – of the spectrum is reachable otherwise in a heterogeneous magnetic field the resonance frequency dispersion causes the peaks spread or even appear as a noise. Therefore, prior to spectrum acquisition it is necessary to homogenize the region of interest through a process called shimming and for the larger ROI it is harder to reach a proper shimming.

1.2.1 Single voxel spectroscopy

In previous section we saw in SVS the spectrum is acquired from a single voxel hence the acquisition is fast. To choose a single voxel three gradients perpendicular to each other (G_x, G_y, G_z) and three selective radio frequency pulses have to be applied so that their intersection provides the volume of interest, Figure 1.7. The first pulse excites a layer in the sample, the next one picks a row of that layer and the last pulse make the voxel by picking a cube of the row [23].

1.2.2 PRESS (point resolved single voxel spectroscopy)

In point resolved single voxel spectroscopy, PRESS, the first 90 degrees RF pulse is followed by two 180 degrees RF pulses and the voxel emits a spin-echo signal. PRESS refocuses the spin using a 180 degrees RF pulse, Figure 1.8.

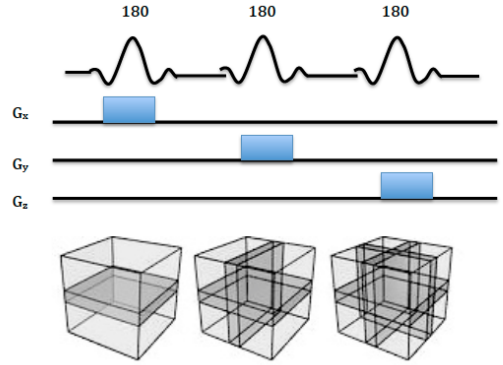

Figure 1.7 – Principal of volume selection

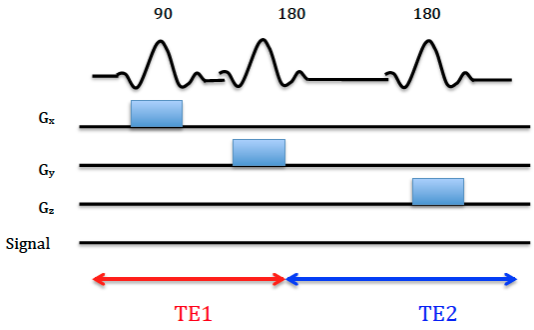

Figure 1.8 – PRESS pulse sequence

1.2.3 STEAM

Stimulated echo acquisition mode, STEAM, is same as the PRESS sequence but all the RF pulses have 90 degrees flip angle. The delay time between the second and third pulse called mix time, TM, and the echo time is double of the time between the first two pulses. However, The signal amplitude is half of the PREESS thus the SNR is half of the PRESS, Figure 1.9.

1.2.4 CSI

Chemical shift imaging acquires data from a group of voxels and works base on the repetition of the PRESS and STEAM sequence accompanied by spatial phase encoding so that the spatial location is phase encoded and spectra is recorded for each phase en-

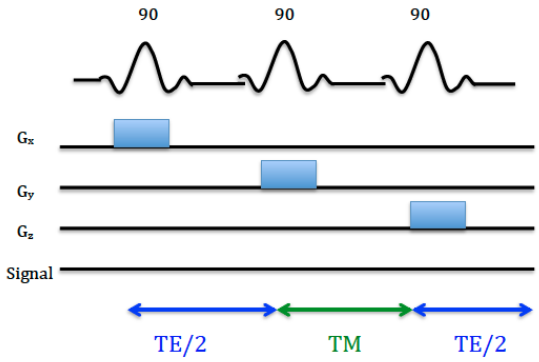

Figure 1.9 – STEAM pulse sequence

coded part. The number of phase encoding pulses as well as their direction depends on the dimension of the interest. For larger number of dimension, the acquisition time will be longer. So the duration time of the sequence is as follow:

$$t_acq = T_R \;\; Np_1D \;\; Np_2D \;\; Np_3D \;\; NSA$$

NSA is the number of signal averages and Np_nD represents the number of phase encoding steps in direction x.

1.2.5 FID

The FID sequence is unlocalized sequence; it collects the signal from all around the sample that is inside of the coil field of view. It is a commonly used sequence in *in vivo* spectroscopy where the subjects exercise in the scanner.

1.3 Energy in Muscle

Muscles are nourished by the oxygen that lungs capture from the air and nutrients present within the blood stream [24]. During exercise muscles go through a series of relaxation and contraction. ATP is the key factor in contraction as it breaks into ADP and Pi. This split lets the muscle contract during a cycle of attachment and detachment between actin and myosin (regulatory protein in muscles) [25]. On the other hand, phos-

phocreatine (PCr) holds high-energy phosphorus bonds and serves as a source of energy which is available on demand. During contraction PCr concentrations decrease to replenish ATP. Another alternative is to regenerate ATP from Adenosine diphosphate (ADP) through oxidative phosphorylation using oxygen from the blood stream. Together, the two mechanisms manage the ATP levels to remain constant [26]. When the workload increases, ATP consumption exceeds its regeneration, which leads to a reduction in pH and acidic cramp of the muscle.

1.3.1 Why phosphorus?

According to previous description, PCr and ATP are the essential energy reservoirs in the biological system and their concentrations vary in each organ. PCr in the brain, heart and skeletal muscle is around 5-6, 10 and 33.5 mM while ATP is 3-4, 6 and 10 mM, respectively. Once the concentrations change they may cause various disease conditions, including muscular disorders, heart infraction and tumors [27]. ^{31}P NMR spectroscopy has been used to study precise metabolic mechanisms and detect the signal from these metabolites. The high natural abundance of phosphorus and its sensitivity (7% of proton) provides a high quality spectrum within minutes of acquisition. Using ^{31}P NMR all the key metabolites could be detected [28]. In the next section we will study these key metabolites in the human calf muscle.

1.3.2 Identification of resonance

The phosphorus spectrum of the human calf muscle contains a large peak representing phosphocreatine (PCr) followed by three non-equivalent phosphate groups of ATP. To the left side of PCr, a signal from inorganic phosphate (Pi) exists and under encouraging circumstances signals from phosphomonoesters and phosphodiesters show up as well [29]. As already addressed in Chapter 1, depending on the chemical environment of each compound, the resonance frequency of the nucleus varies. Therefore, the spectrum of the phosphate chemical content of the muscle is its fingerprint. Figure 1.10 shows the resting ^{31}P spectrum from human calf muscle.

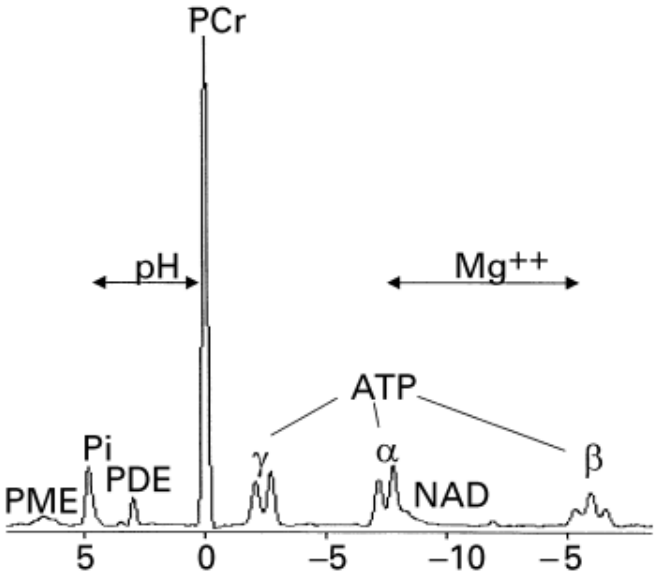

Figure 1.10 – ^{31}P spectrum of a human calf muscle acquired within 3T magnetic field represented in ppm scale, Figure taken from [2].

For *in vivo* spectroscopy PCr frequency position is chosen as the chemical reference frequency. 0.00 ppm is the assigned chemical shift value. Tabel 1.I gives the chemical shift of the observable nucleus all around the ^{31}P spectrum.

A detailed observation of ^{31}P spectrum of skeletal muscle discloses fine detailed information of phosphorus spins. As described in section 1.6, the mutual interaction between nuclear spins could take place between neighboring phosphorus atoms or protons. The peak splitting in γ-ATP, α-ATP and β-ATP is due to the J coupling phenomena [30]. In other words, the phosphate-phosphate spin coupling and proton-phosphate spin coupling reveals itself in phosphomonoesters, phosphodiesters and diphosphodiester.

1.3.3 Intracellular pH

The chemical shift of the metabolite containing phosphorus depends on some physiological parameters such as Magnesium concentration and intracellular pH. The variation of the intracellular pH originates from the protonation of the compounds and it alters the chemical environment and consequently the chemical shift of the compounds. As an example, consider a solution holding two different pH values but identical biochemical

Table 1.I – Chemical shift of ^{31}P containing metabolites.

Compound		^{31}P chemical shift (ppm)
Adenosin monophosphate (AMP)		6.33
Adenosin diophosphate (ADP)	α	-7.05
	β	-3.09
Adenosin triphosphate (ATP)	α	-7.52
	β	-16.26
	γ	-2.48
Phosphocreatine		0.00
Inorganic phosphoate		5.02

compounds; ATP, PCr and Pi. The effect of the variation of intracellular pH emerges as a observable shift in the peak's position on the frequency axis, Figure 1.11.

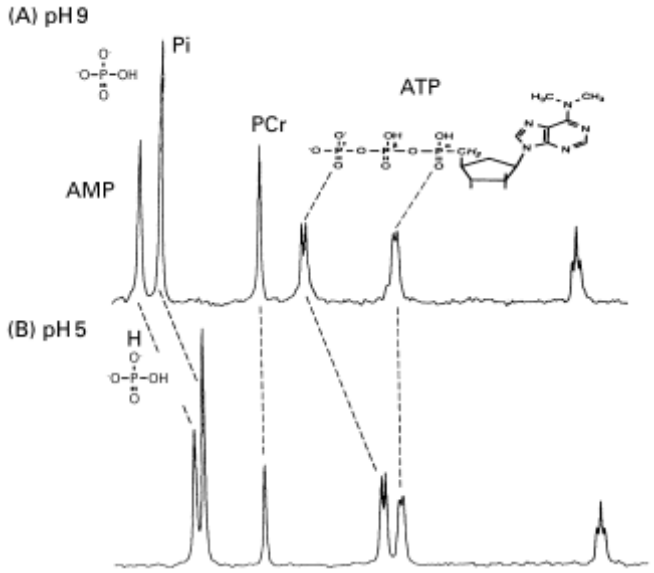

Figure 1.11 – Displacement of the physiological ^{31}P containing metabolites by pH variation, Figure taken from [2].

Intracellular pH is related to the pi-PCr shift. Another physiological parameter that is able to change the resonance frequency position is Mg^{2+}. Particularly β-ATP is the one that mostly dependent on Mg^{2+} content [31].

During the exercises and muscle contraction ATP has to be broken and releases free

energy. Muscles use this energy to contract based on the [32]:

$$ATP \rightarrow ADP + Pi + energy \rightarrow \text{Muscle contraction} \tag{1.30}$$

ATP together with ADP, AMP(adenosine monophosphate) and Pi are essential factors for muscle cells to function properly. Once concentrations of ATP decrease, cells rapidly develop fatigue – defined as a depletion of ATP turnover through the skeletal muscle – that consequently reduces the ability of muscle to produce power. Fatigue is an important physiological process that prevents ATP from dropping too low, leading to irreversible damage. By ATP reduction, cells start to compensate for the ATP shortage and demands for its increase. Cells regenerate ATP throughout three systems [33]:

— phosphagen system

— Glycolytic system

— Mitochondrial respiration ...

However, the first system, phosphagen, has the largest contribution in terms of the regeneration rate of ATP and its intensity. In the following we will see how the phosphagen system supplies human body metabolism.

1.3.4 The phosphagen system in muscle

The phosphagen system can be expressed in three reactions:

$$PCr + ADP + H^+ \rightarrow ATP + Cr \qquad \text{Creatine kinase} \tag{1.31}$$

$$ADP + ADP \rightarrow ATP + AMP \qquad \text{Adenylate kinase} \tag{1.32}$$

$$AMP + H^+ \rightarrow IMP + NH_4^+ \qquad \text{AMP daminase} \tag{1.33}$$

The first and second reaction, creatine kinase and adenylate kinase, both regenerate ATP, although the majority of the ATP is produced by creatine kinase. The last reaction does not regenerate ATP, however, it is a part of the phosphagen system that shows how AMP converts to IMP(inosine monophosphate). During hard exercise the energy released by the phosphagen system will continue until PCr is considerably reduced. PCr decreases

rapidly and depletion may occur within the first 10 seconds of exercise [25]. That is why most of the intense exercise and sports includes some recovery intervals. Research reveals that the recovery time needed for full compensation of PCr may take as long as 5 to 15 minutes [34], [35]. Figure 1.12 shows the PCr concentration in muscle in resting state and its depletion through exercise [26].

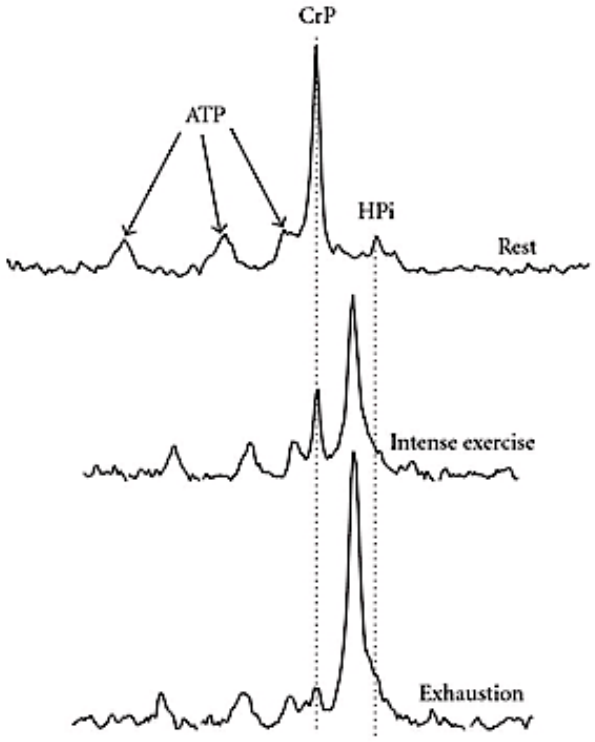

Figure 1.12 – The top shows the ^{31}P NMR spectrum of muscle at resting state, muscle at near complete PCr depletion, and muscle with complete PCr depletion, Figure taken from [2].

Figure 1.12 demonstrates how PCr depletes during the exercise phase. The first image shows the phosphorus spectra at resting state. In the next stage, PCr is close to complete depletion. In the last spectra PCr is completely depleted. Simultaneously, inorganic phosphate increases and the position of the resonance frequency moves to right – the chemical shift increase – and the pH increases, which leads to muscle acidosis.

1.3.5 Calf muscle

In human body the calf muscle is located on the back of the lower leg and actually consists of two muscles; gastrocnemius and soleus. Gastrocnemius is the largest of the two muscles. The soleus forms the smaller part; a flat muscle positioned beneath the gastrocnemius muscle. The soleus and gastrocnemius muscles are both involved in plantar flexion exercise. We chose calf muscle as a desired organ to conduct ^{31}P spectroscopy, Figure 1.13.

Figure 1.13 – Axial view of the calf muscle using 3T Siemens MR scanner, image taken during study.

1.4 RF Coil

To transmit an oscillating magnetic field and receive the resultant RF signal we have to use a resonator or radio frequency coil –RF coil. During the transmission phase, RF coil terminals receive a high power electrical signal and form a current in the coil conductors. Based on the Faraday's law this current induces a magnetic field B_1 that oscillates at the RF input frequency. In the receive mode the magnetization vectors inside the sample precess and consequently change the flux within the coil. Once the flux changes – based on Faraday's law – it induces an electromotive force, emf, in the

coil. In fact, the spectrum that we are interested in is this emf, which is amplified and passed through fast Fourier transformation [36].

Surface coils are one of the simplest types of coils able to produce and detect magnetic fields. Although it is not the most efficient, as the produced magnetic field is very inhomogeneous, they are linearly polarized and they can provide higher SNR compared to volume coils because surface coil positions very close to the region of interest, ROI.

Bio-Savart's law is an analytical model that describes how an electrical current induces a magnetic field in a loop. To calculate the magnetic field, a steady current (Idl') has to be defined and integrated over a closed path of current. The magnetic field can be calculated by:

$$dB = \frac{\mu_0}{4\pi} \oint \frac{I\, dl' \times \hat{\mathbf{r}}}{r^2} \tag{1.34}$$

r is the full displacement vector from the loop element to the field point. $\hat{\mathbf{r}}$ is the unit vector of r, which is the unit displacement vector between the current element and the observation point. For instance, consider a closed loop with the radius of a carrying a constant current I. To calculate the magnetic field of this loop, by Eq. 1.34, the magnetic field sweeps out of the loop and makes a cone, Figure 1.14. The horizontal components of the magnetic field is canceled out and the vertical component adds up to:

$$B(z) = \frac{\mu_0}{4\pi} \oint \frac{I\, dl'}{r^2} \cos(\theta) \tag{1.35}$$

$$B(z) = \frac{\mu_0}{4\pi} \frac{I(2\pi a)}{r^2} \cos(\theta) \tag{1.36}$$

Given that $r^2 = a^2 + z^2$ and $cos(\theta) = a/(a^2+z^2)^{1/2}$

$$B(z) = \frac{\mu_0\, I}{2} \frac{a}{(a^2+z^2)^{\frac{3}{2}}} \tag{1.37}$$

Eq. 1.37 gives the magnetic field at any distance from the loop. The strength of the field decreases as the distance from the center of the coil increases. Based on Lenz's law any flowing current is capable of creating a magnetic field in the loop. If the current

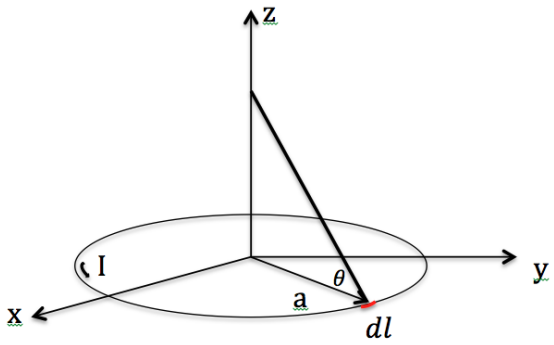

Figure 1.14 – Magnetic field of a loop.

is applied at the resonance frequency of the coil the induced magnetic field is much stronger. At the resonance frequency the imaginary parts of the impedance of the loop are canceled out and the impedance is pure resistance. The impedance of the coil is calculated by:

$$Z = j\omega L + \frac{1}{j\omega C} \tag{1.38}$$

Here L is the inductance of the coil and C is the capacitors on it.

1.4.1 Transmission line

To propagate the signal through the sample and transmit the power between the coil elements, transmission lines are necessary. The transmission line in RF coils are normally coaxial cables that have 50 Ohms impedance. Figure 1.16 shows how a wave

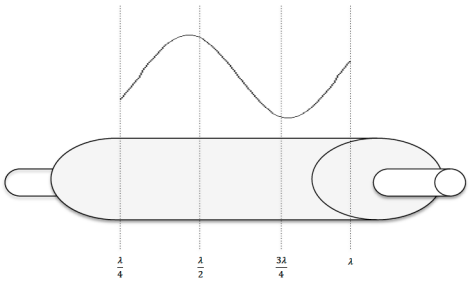

Figure 1.15 – RF signal wave length and the coax length.

propagates within a cable. Once the wave enters a load it divides into two parts; transmission and reflection. The transmission lines ending with their nominal impedance

only have a transmission component and do not reflect any portion of the wave back to the source. This is an important fact called matching that we will describe in more detail in section 3.4.

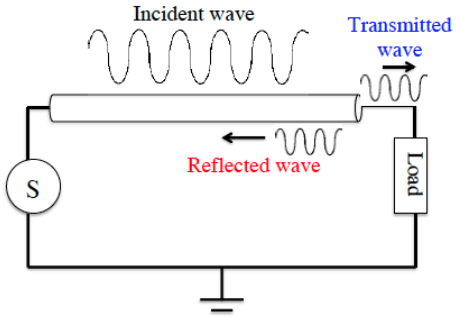

Figure 1.16 – Signal propagation in inside a transmission line [2].

The reflection coefficient describes the amount of the wave reflected back to the source as a ratio of the electric wave voltage and the regressive wave.

$$\Gamma = \frac{(\overline{V}_+)}{(\overline{V}_-)} \tag{1.39}$$

The impedance of the load at the end of the transmission line can be defined as

$$Z_L = Z_0 \frac{\overline{V}_+(0) + \overline{V}_-(0)}{\overline{V}_+(0) - \overline{V}_-(0)} \tag{1.40}$$

while Z_0 is the characteristic transmission line impedance, the reflection coefficient can be rewritten as Eq. 1.41 that measures the amplitude of the reflected wave compared to the amplitude of the incident wave.

$$\Gamma = \frac{Z_{charge} - Z_0}{Z_{charge} + Z_0} \tag{1.41}$$

In fact, the easier way to measure the amount of reflection is using the standing wave ratio, SWR, that measures the maximum voltage to the minimum voltage of the line. The voltage is at a maximum when the incident and reflected waves are in phase and at a minimum when they are out of phase. The equation of SWR can be easily rewritten in

terms of the reflection coefficient.

$$SWR = \frac{|V_+(0)| + |V_-(0)|}{|V_+(0)| - |V_-(0)|} \tag{1.42}$$

$$SWR = \frac{1 - |\Gamma|}{1 + |\Gamma|} \tag{1.43}$$

SWR directly describes at which point the line impedance is matched to the load. For those circuits that are perfectly matched, SWR equals one. A network analyzer measures the amount of power reflection and transmission by its scattering ports. The S_{11} port in a network analyzer represents the reflection coefficient from the coil. As an example, if S_{11} = 0 dB it means all the power is reflected back to the source power and no power is radiated to the coil. The larger return loss means the amount of reflection is smaller than the transmission. In surface coils we are aiming to have a S_{11} parameter of around -20 dB.

$$Return\ \ loss = -20\ log\Gamma = -20\ log\frac{Z_{load} - Z_0}{Z_{load} + Z_0} \tag{1.44}$$

Coaxial cable is the most commonly used transmission line. However, they hold un-

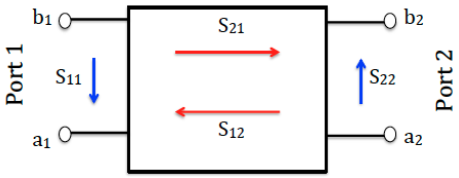

Figure 1.17 – Network analyzer ports.

wanted common mode current and also attenuate the signal all along their way to the coil. Common mode currents cause an external coupling between the coils and radiation. It has been shown that the shorter length of the cable may reduce the amount of loss and suppress the common mode [37].

1.4.2 RLC circuit

A circuit consisting of resistance, capacitors and inductors could be arranged such that it resonates at a specific frequency. To do so, an RLC circuit should satisfy the

equation below, while q is the electric charge flowing in the circuit and induces an emf, E(t):

$$L_t \frac{(d^2q)}{(dt^2)} + R_t \frac{dq}{dt} + \frac{q}{C_t} = E(t) \tag{1.45}$$

solving the second order equation gives:

$$q(t) = Asin(\omega_0 t + \theta) \tag{1.46}$$

while $\omega_0 = 1\sqrt{(L_t C_t)}$, R_t,L_t and C_t are total resistance, total inductance and total capacitance, respectively. Normally the R_t is desired to be as low as possible to have the least loss and L_t is the intrinsic inductance. By choosing the proper capacitors the coil resonates at the desired frequency [38, Ch. 1, p. 6]. Another approach to acquire resonance frequency is the total impedance of the circuit. For an RLC circuit the impedance of each element is R, $j\omega L$ and $1/j\omega C$ and is dependent on their arrangement; series or parallel. The total impedance of the circuit is given by:

$$\overline{Z_t} = \sum_k \overline{Z_k} \tag{1.47}$$

$$\overline{Y_t} = \sum_k \overline{Y_k} \tag{1.48}$$

While $Y_t = \frac{1}{Z_t}$ and the former equation can be written as

$$\frac{1}{\overline{Z_t}} = \sum_k \frac{1}{\overline{Z_k}} \tag{1.49}$$

In the aforementioned scheme for the ^{31}P surface coil, an RLC circuit is in series, so the total impedance will be

$$\overline{Z_a} = R_t + i(\omega L_t - \frac{1}{\omega C_t}) \tag{1.50}$$

If the imaginary part is canceled then the coil has the minimum impedance. In other words, the largest current will flow within the coil at the Larmor frequency which is

calculated as Eq. 1.51.

$$\omega_0 = \frac{1}{\sqrt{LC}} \tag{1.51}$$

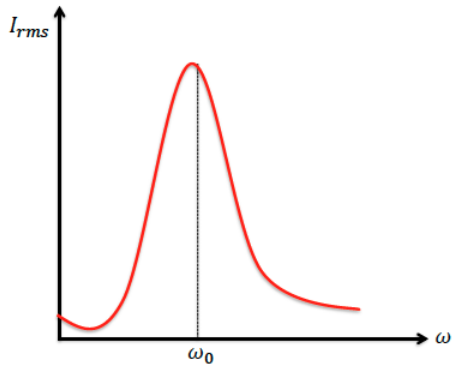

Figure 1.18 – Highest power transmission at Larmour frequency.

1.4.3 Impedance matching

The previous section explained how a resonance frequency provides the coil with a pure resistive behavior. However, the exact value of the impedance also depends on the resistance of the target tissue and metabolic constituents. To transfer the energy optimally from the coil to the target tissue (and the other way around) the impedance of the RF coil must be matched to the impedance of the transmission line, which is 50 Ohms. It is not feasible to do impedance matching for each single subject or phantom; instead the impedance matching can be done using a phantom containing the typical constituent of the tissue of interest. Consequently we assume that the coil is in its optimal condition to transmit and receive the RF signal. In the coils that lack a proper matching, a large fraction of the RF power generated will not be transmitted into the target as it should be, instead it will be reflected back at the coil transmission line interface to the power source. In next section we will see how a method called a Smith chart aids us to reach the 50 Ohms matching.

1.4.3.1 Smith chart

The Smith chart is the most commonly used graphical chart in RF communication. The calculation is required to observe the mutual conversion between the load impedance and the reflection coefficient. Impedance circles and reactance curves mainly constitute the Smith chart as shown in Figure 1.19. Each load impedance could be shown as a dot on the chart with a specific resistance and reactance.

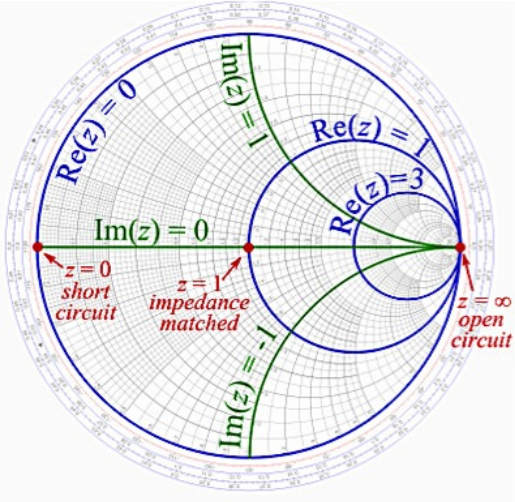

Figure 1.19 – Smith chart.

As we discussed before, the ideal operation point of the coil is where the load impedance equals the intrinsic impedance of the transmission line, 50 Ohms. At the center of the chart the reflection coefficient is zero as $\frac{Z_{load}}{Z_0}$ equals one. To have the minimum reflection the impedance of the load has to reach the center of the chart where the load becomes the real resistance with null reactance.

CHAPTER 2

METHOD

2.1 Coil construction

The growing demand for multi-nuclear NMR spectroscopy along with a proton nuclei channel for localization and shimming requires non-proton MR probes that perform with high sensitivity. It is more common to use a Tx-Rx switch between transmitter and receiver elements. However, the use of two separate loops, one for transmitter and the other for receiver, allows a free switch coil. This chapter describes different elements of 1Tx-1Rx ^{31}P surface coils, including the steps for design, fabrication and validation.

2.1.1 Receiver

A dipole magnetic coil, called a surface coil, is commonly used to receive RF signals. Volume coils also are able to receive RF signals, however, surface coils can be positioned closer to the ROI and provide higher SNR. On the other hand, volume coils benefit from a more homogeneous magnetic field. In cases where an array of the surface coils receive the signal, each element should be decoupled from the others. Otherwise the impedance will consequently change as well as the resonance frequency. To tackle this problem the elements have to be decoupled using geometric decoupling, such that the center of the circular loops should be at the distance of 0.78 times the loop diameter. For the square loops, the distance between the centers is 0.86 times the linear dimension in which the coils are overlapped. At this point the mutual inductance becomes zero.

Considering that the RF coil has two separate loops (transmitter and receiver), to avoid signal interferences the loops must be mutually decoupled. Most of the decoupling strategy uses the active switching of PIN diodes as shown in Figure 2.1. During the transmission of the T_x loop, the diode on the R_x loop has a forward bias; this leads to a parallel circuit between L and C. This parallel circuit, in cooperation with the loop of the coil, induces a resonance frequency so it resonates in another frequency instead of

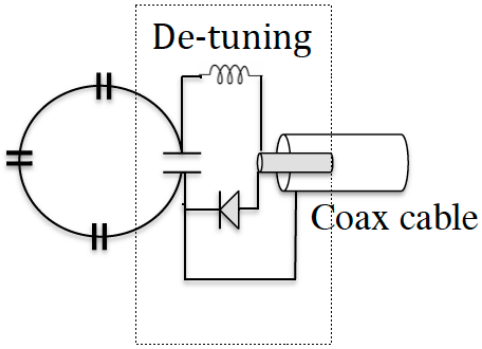

Figure 2.1 – RLC circuit of the receive loop.

the Larmor frequency. In receive mode the diode is biased reversely so the circuit will be open and the coil will resonate at the desired frequency.

2.1.1.1 Signal to noise ratio, SNR

It has been shown that there are two major sources of noise in MRI [39]. The first one is the eddy current that is magnetically induced in the sample. The second one is the losses due to series inner wire resistance of the receiver coil. Thus the loss function can be formulated as:

$$SNR \propto \frac{\omega^2 B_1}{\sqrt{r_{coil} + r_{sample}}} \tag{2.1}$$

r_{coil} is the total resistance of the coil and r_{sample} represents the effect of the sample on the receiver coil. In the receiver coil, assuming that a larger transmitter induces a more homogeneous magnetic field, the B_1 is the principal factor in SNR. For a single loop of the receiver coil, B_1 is calculated as

$$Signal \propto \omega^2 B_1(z,a) \propto \frac{(\omega^2 a^2)}{(\sqrt{a^2+z^2})^3} \tag{2.2}$$

The coil sensitivity decreases as the distance from the coil increases and those tissues that are closest to the coil contribute the most to r_{sample}. The effective dimension of the tissue that the coil detects depends on the coil radius, a. The sample resistance

contributing to the loss is given by:

$$r_{sample} = \omega^2 f(a) \tag{2.3}$$

$f(a)$ is a geometry function of the coil radius and by increasing the size of the coil $f(a)$ grows rapidly. That is why smaller coils provide larger SNR. It has been shown that in surface coils, r_{sample} can be nine times greater than r_{coil}. By neglecting the r_{coil} SNR is rewritten as

$$SNR \propto \frac{\omega}{a\sqrt{f(a)}} \left[\frac{a^2}{(a^2+z^2)^3}\right] \tag{2.4}$$

The first term shows that a larger coil lacks the lower SNR and the second term shows that SNR drops as the distance from the loop increases. Thus, SNR for a surface coil depends more on the coil geometry than the tissue volume.

2.1.1.2 Preamplifier

The received signal from the tissue is very weak so it needs to be amplified on the receiver side. To do so a low noise preamplifier (LNA) tuned to the Larmor frequency, is used (it will be referred to as simply a preamp). The commercial preamplifier, as well as the ones we used, magnifies the signal by factor of 1000, or 30 dB. Other types which amplify by factor of 20 dB are also available.

$$G(dB) = 10\ log\ \frac{P_{output}}{P_{input}} \tag{2.5}$$

$$G(dB) = 10\ log\ 1000 = 30\ \ dB \tag{2.6}$$

The preamps we used were initially tuned to proton frequency. To make them operate at phosphorus frequency we changed their resonance frequency by adding capacitors and inductors the gain reduced to 25 dB. The noise factor (NF) is calculated by the logarithmic difference of the noise output with the real receiver and noise from an ideal receiver. The commercial preamps have an NF lower than 0.5 dB, which decreases SNR. On the other hand it reduces the amount of noise coming from the transmission line if it

is positioned as close as possible to the source.

$$NF(dB) = 10\ log\ \frac{Noise_{output}}{G.Noise_{input}} \tag{2.7}$$

Port S_{21} on a network analyzer measures the amplification gain such that port S_2 transmits the signal to the preamp and port S_1 receives the amplified signal after it passes through the preamp. Given that the intrinsic power of the coil is quite low, around μV, using the preamp the power increases to mV.

2.1.2 Transmitter

The transmitter coil inside the MR machine excites the spins in the sample. It induces the B_1 magnetic field, which disturbs the spins with the desired frequency. The proposed structure for the transmitter is same as the receiver; a single loop tuned to ^{31}P frequency. It has a larger diameter and a matching circuit on the loop. The larger diameter for the transmitter allows us to excite deeper tissues and provide more homogeneous magnetic field for the receiver.

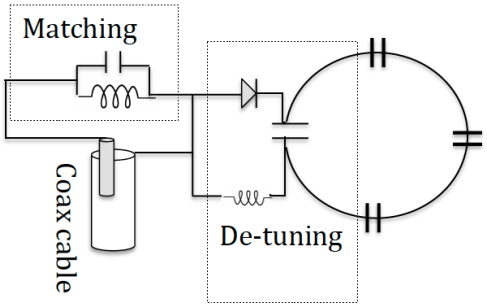

Figure 2.2 – RLC circuit of the transmit loop, detuning and matching circuit of it.

2.1.2.1 SAR calculation

Specific absorption rate (SAR) is the amount of RF power absorbed per unit of sample mass. It describes the vulnerability of the tissue to heating due to RF energy. It is

measured in units of (watts/kilogram). When RF energy is transmitted into the tissue, it causes the ROI to heat. In high enough energy the tissue may be damaged. The SAR value should thus be kept low; for the field strength of the 1.5T, the SAR is quite low and a negligible amount of RF is absorbed by the tissue. However for a 3 Tesla, the higher frequency will increase the absorption of the energy and SAR will be quadrupled. Food and Drug Administration (FDA, USA), has defined SAR limits. It has been suggested that the limit for the MR machine is 3 W/kg averaged over the whole head in 10 min, 4 W/kg averaged over the whole body in 15 min, or 8 W/kg per gram of head/torso tissue in 5 min or 12 W/kg per gram of extremity tissue over 5 min as the normal mode limit [40].

2.1.3 Detuning

Given that transmitter and receiver coils resonate at the same frequency they have to operate independently. Diodes are the principal component in the detuning circuit, so that depending on the bias direction – forward or inverse– allows only one of the loops to operate at a time. The detuning circuits could be positioned anywhere on the loop coil; for the transmitter and receiver we put them as a simple series circuit on the loop. When the diode is forward biased the current circulates only in the detuning circuit and not in the loop, thus the coil resonates in another frequency, which is far from the phosphorus Larmor frequency.

2.2 Coil fabrication

During spectroscopy experiments the coil is positioned under the sample and should withstand the weight. An important aspect of the coil's design concerns the stability. To prevent any breakage and mis-connection we designed a box and printed precisely. The printer is Elite 3D of the economy size that uses acrylonitrile butadiene styrene (ABS). It is a relatively rigid thermoplastic, resistant to shocks, light-weighted and MR compatible. A box with a curve surface, a wall, a disc and a bottom surface was printed. The parts have been designed with a slide system such that they hold together tightly.

The coil has one receiving element that we want to be positioned as close as possible to the target sample. The curved surface of the box, on the top, is located under the sample holder – calf muscle or phantom. Using small screws we attached the receiver element on the under side of the curve surface. The transmitter loop is positioned on the disc as close as possible to the receiver. The PCB board holding the cable traps (to block the proton frequency during ^{31}P spectroscopy) and preamp was screwed to the bottom of the box.

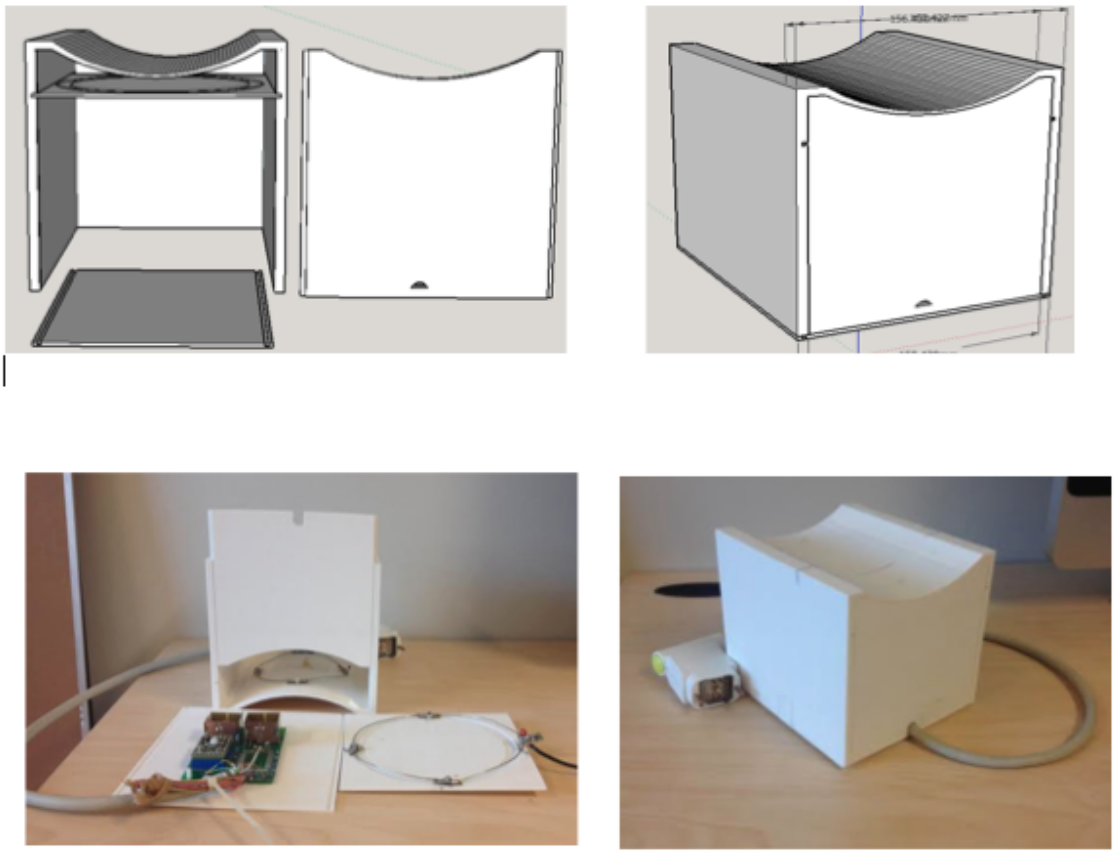

Figure 2.3 – Up: Three dimensional sketch of the box to support the coil. Down: 1Tx-1Rx Rf surface for ^{31}P spectroscopy.

2.3 Bench measurement

To make sure elements are workings well together, a series of bench measurements needed to be performed.

The receiving and transmitting elements and detuning circuit were individually tuned to 49.8719 MHz. To tune the coil, four capacitors were located on the loop and using the S_{11} port of the network analyzer we observed the resonance frequency. Given the capacitors value as well as the resonance frequency we are able to calculate the inductance of the loop using Eq. 1.51. Knowing the inductance of the loop and the Larmor frequency, the right value of the capacitors could then be calculated to reach the desired frequency. Next, to reach an impedance of 50 Ohms at the end of the transmission line, a parallel circuit of the inductors and capacitor is considered. The impedance was adjusted by changing the value of the capacitors and inductors of the matching circuit. An example of tuning and matching results obtained for the relative magnitude of the signal and resonance frequency is shown in Figure 2.3. These measurements were taken in S_{11} mode while one end of the coaxial cable went to the coil and the other was connected to the input terminal of the network analyzer. Considering the preamp already tuned to 50 Ohms we didn't consider it in matching. The network analyzer should take into account the length of the coaxial cable, so a calibration should be performed with the same cable length prior to tuning and matching. The tuning and matching is performed separately for R_x and T_x.

The following steps must be taken to assure the effectiveness of the detuning circuit. The receiver element should not absorb the RF energy when the transmitter is sending power. The same is true for the transmitter when the receiver is operating. To see the isolation between the loops a S_{21} measurement is performed using two geometrically decoupled loops. The probe is placed around the receiving element when it is idle and when it is active mode. The isolation between the transmitter and receiver loop was perfectly achieved and the detuned state for them is shown in Table2.I.

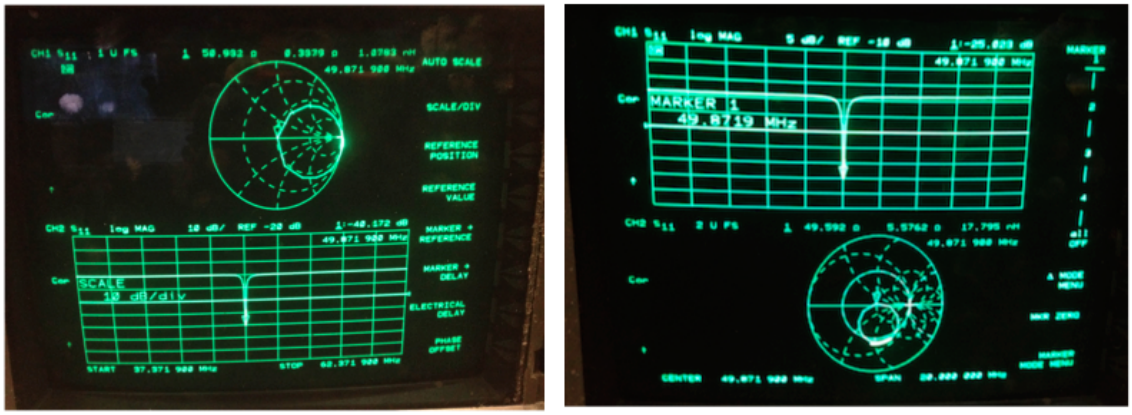

Figure 2.4 – S11 measurements of each loop; Right: Receiver, Left: Transmitter.

Loop	Isolation	Tuned	Detuned
Transmitter	-33 dB	25 dB	-18 dB
Receiver	-33 dB	26 dB	-17 dB

Table 2.I – Isolation between tuned and detuned loop

2.4 Voltage calibration

Once the setup is perfectly matched and tuned, the MR scanner is used to execute two sets of ^{31}P spectroscopy. First, *in vitro* ^{31}P spectroscopy using two phantoms containing different phosphorus concentrations, 10 mM and 100 mM respectively. Second, *in vivo* ^{31}P spectroscopy on the calf muscle of healthy subjects during resting state and during exercise. The aim of this chapter is to use MR images and spectra as an indication of coil performance. We will also discuss the methodology and tasks –prior to and during the experiment– required to perform spectroscopy using a 3 Tesla MR scanner.

For the commercial coils, the MR scanner sends a voltage through the transmitter so that the receiver acquires the highest signal intensity from the desired voxel. For the hand-made coils the user has to obtain this optimum voltage manually, or include this task in the pulse sequence for greater efficiency. Therefore, prior to testing the coil on the phantom, or the subject, a voltage calibration needs to be performed. To do so the coil is positioned on the phantom and using a fid sequence the voltage is gradually increased starting from 10 volts up to 200 volts with incremental steps of 10 volts. Through this

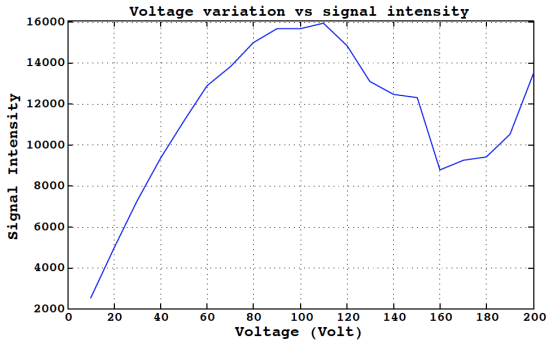

Figure 2.5 – Voltage variation profile of 100mM phantom.

procedure T_R was quite long and T_E was relatively short. We aim to find the smallest power entry, which provides the largest possible signal and expect a curve that follows a sine wave. The signal intensity increases with voltage increments up to V_{opt}. This gives the true 90 degrees excitation. Once excitation exceeds 90 degrees and V_{opt} is passed, the signal intensity drops. At $2 \times V_{opt}$ the flip angle is 180 degrees and the spins stay in the same direction and absorb enough energy to change from parallel to anti-parallel orientation. For the 100 mM phantom the optimum voltage equals 70 volts and for the rest of the experiments on this phantom we will use this as the reference voltage.

2.5 Depth of penetration

We already saw that the excitation is stronger for tissues closer to the coil. It has been shown that the depth of the penetration for a loop is almost equal to its radius [37]. The transmitter loop with the larger diameter (14.5 cm) excites a slice with thickness of up to 7.25 cm. The receiver (11 cm) collects the signal from the slices, up to 5.5 cm thickness. We chose the smaller receiver to precisely acquire the signals, for the smaller ROI. The dimensions are appropriate for studying various sizes of calf muscle as well as fat thickness across different subjects.

2.6 *In vitro* spectroscopy

Once the bench tests and voltage optimization are successfully performed, to validate the hardware and sequences designed for the phosphorus spectroscopy we aim to implement *in vitro* tests.

2.6.1 Phantom

Phantoms are the main element in *in vitro* testing. They are especially useful during the SAR calculation, voltage calibration. Also, with prior knowledge of the phantom concentration a quantitative measurement can be performed. The phantoms for the *in vitro* testing were made based on the recommendations from Provencher [41] –used in proton spectroscopy. A buffer solution containing potassium phosphate and salts provides a total concentration of PO_4 of 100 mM. To evaluate the coil response in detecting a phosphorus signal two phantoms are required. One has a higher concentration of phosphorus metabolites, 100 mM. While the other phantom contained a lower concentration, 10 mM. The low-concentrated phantom was intended to simulate the phosphate concentration of the same order of magnitude of the one found in the human body.

Figure 2.6 – *In vitro* spectroscopy.

2.6.2 Positioning in the scanner

During the phantom test, the curved surface of the coil box which holds the receiver is located under the phantom, as shown in Figure 2.6. Phantoms are preserved in a fridge to prevent any chemical degradation. One hour before testing they are removed to let them reach room temperature.

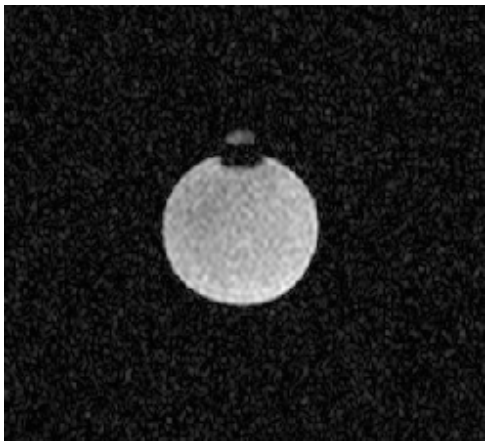

Figure 2.7 – Proton image of the phantom.

Velcro is used to wrap the coil to the phantom to help prevent movement. To locate the coil coordinates, a small pill is positioned at the center of the receiver. Figure 2.7 shows the anatomical image of the phantom captured by proton imaging. The small white spot represents the pill and consequently the coil location on the phantom. The black space between the pill and the phantom is air bubbles; to avoid them we put small wedges beneath the top of the bottle to help tilt it.

2.6.3 3D Shimming

The next step is to shim the local magnetic field. This homogenizes the magnetic field over the desired area of the volume and obtains the best possible Lorentzian line shape for various resonance peaks over the spectrum. A proper shim provides a FWHM of less than 25 Hz for 3D MRSI. This provides better water suppression, which is crucial in proton spectroscopy as well as a precise peak separation. The resulting field map over the sample is shown in sagittal view. Doing that the system calculates the currents

required in the gradient coil to provide the optimal homogeneity over the spectroscopic ROI. Normally a couple of measurements is required to reach optimal shimming.

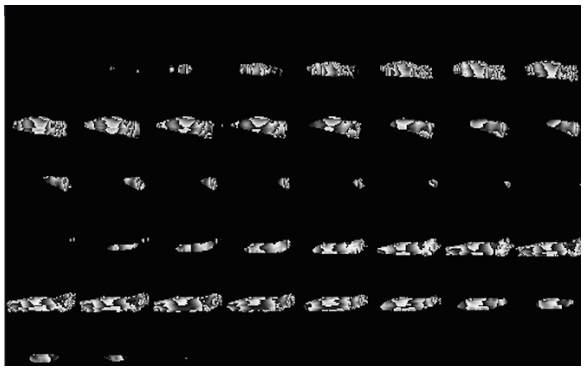

Figure 2.8 – Localized automated shim illustration of human calf muscle.

Since we intend to run ^{31}P spectroscopy we need to introduce the exact frequency of the desired compound to the MR machine. To do so in the *X-frequency* section we defined the exact resonance frequency. The Larmor frequency of phosphorus in a 3 Tesla external magnetic field is 51.7 MHz. It is interesting to note that Siemens MR scanners are not exactly 3 Tesla but 2.89 Tesla. This slight difference significantly changes the Larmor frequency. Considering the actual strength field of 2.89 MHz the ^{31}P resonance frequency is calculated as follows:

$$f = \frac{\gamma}{2\pi} B = 17.235 \times 2.89 = 49.8719\, MHz \tag{2.8}$$

Lastly, to have the strongest signal intensity the optimum voltage (section 5.2) needs to be imported as the reference amplitude in the transmitter section. Figure 2.9 demonstrates the phosphorus spectrum of the phantom acquired by the single voxel spectroscopy sequence. The voxel size was $4 \times 4 \times 4$ cm and T_R= 1500 and T_E=15 ms. Data collected was processed in jMRUI and MATLAB. The spectrum shows the real part of the data and underwent phase correction before plotting.

Another sequence provided by Siemens is 3D chemical shift imaging, discussed in section 1.7.4, which acquires the signals from a group of voxels. Without changing the coil place from the previous section the 3D CSI applied. Each single voxel size is

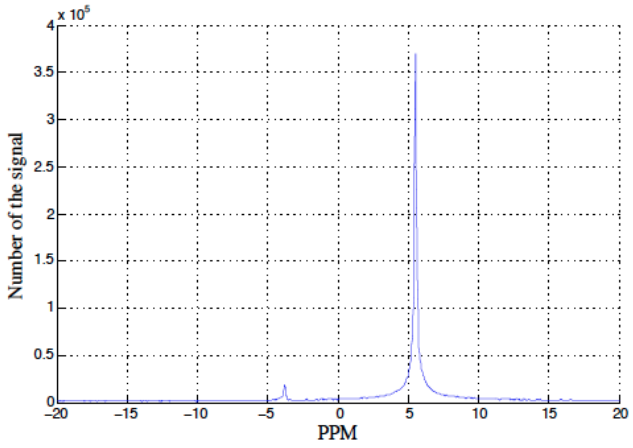

Figure 2.9 – Single voxel spectrum of the 100mM phantom.

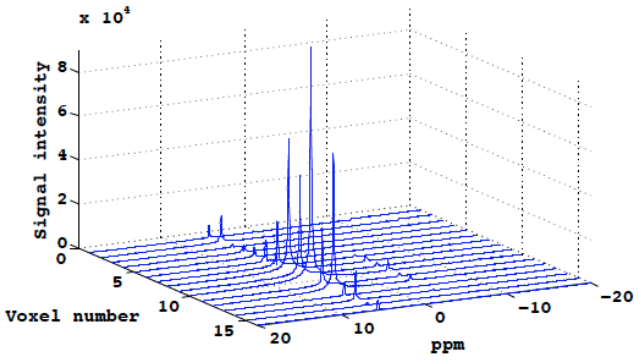

Figure 2.10 – Spectral map generated by 3D CSI measurement.

$25 \times 25 \times 25$ mm, $T_R = 1000$, $T_E = 2.3$ ms and 16 signals of 16 voxels were collected. The highest peak is closest to the center of the coil. As the distance increases from the center of the coil the signal intensity decreases. That is why different voxel locations in Figure2.10 represent various signal intensities. Inverse Fourier transformation of the data provides us with Figure 2.11 – FID signals. It is worth noting that the area under the peak of the spectrum equals the metabolite concentration and FID amplitude.

The next image, Figure 2.10, is the same phantom using phosphorus imaging with the surface coil and FLASH sequence. The image shows only the spatial image of the phantom. The coil could penetrate to the depth of 3.35 cm. It verifies the rule of thumb

stating that the coil depth of penetration is almost the same as the loop radius [42]. The radius of the receiver is 5 cm.

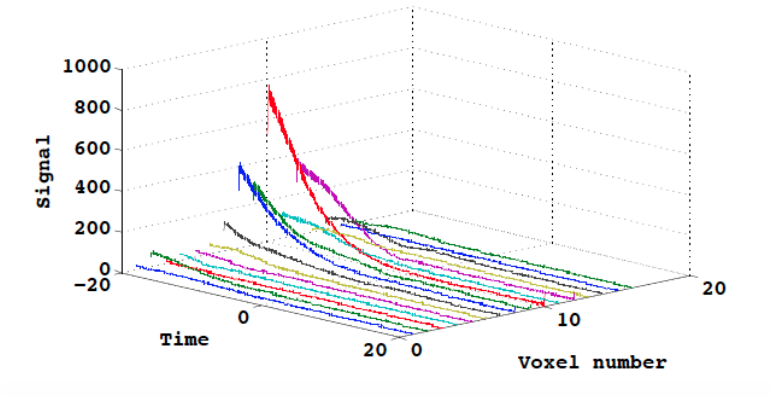

Figure 2.11 – Time profile of the 3D CSI measurement.

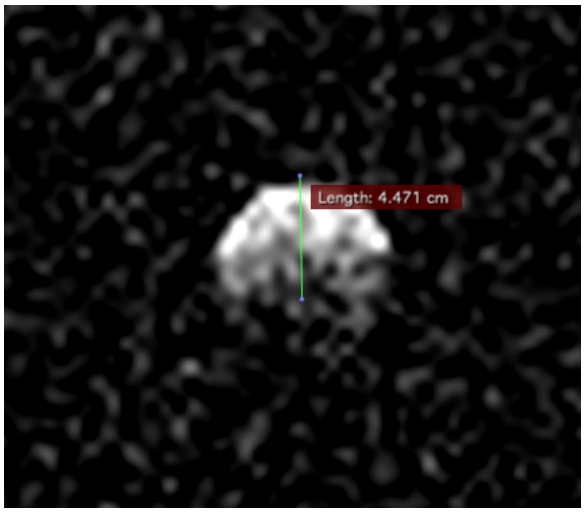

Figure 2.12 – Flash image of the phantom in axial view.

CHAPTER 3

RESULTS AND DISCUSSION

3.1 *In vivo*

When the surface coil succeeded *in vitro* tests, as the next step we performed *in vivo* tests. Given that calf muscle posses the highest concentration of phosphocreatine, 35 mM, and adenosine triphosphate, 10 mM, in human body organs, we chose this muscle to run *in vivo* experiments. To do that, the largest part of the calf muscle of the left leg positioned on the center of the coil.

3.1.1 Experimental protocol

l Five young healthy subjects with a median age of 30 years (range, 24-32 years) participated in the experiment. None of them was specifically trained in sports. The subjects were asked to lie down on the MRI bed with their left leg positioned on the coil. The leg was wrapped to the coil using Velcro to make sure that the target muscle stays on the coil surface. One additional wide strap was placed under the knee and on the lower leg to help stabilize both legs to the MRI bed. A resistance band was used during the experiment. One end was restrained to the dorsum of the foot with a 7 cm wide loop. The subjects were asked to hold the other end of the band in their left hand and pull it up to their chest to increase resistance. This exercise puts pressure on the calf muscle. Exercises were performed at a constant frequency of 30 plantar per minute.

3.1.2 Exercise protocol

To find the optimum protocol each volunteer performed a different exercise protocol during ^{31}P MRS measurement: The first subject, after 1 minute of rest, performed an exercise protocol which consisted of 6 minutes of consecutive exercise and a recovery time of 4 minutes. The T_R was 1850 with a number of averages of 64, Figure 3.3. The second subject did two separate protocols. The first one, 1 minute of rest was followed

by one exercise session of 6 minutes with a 5 minute recovery. In the second protocol the subject exercised for three intervals of 4 minutes with a 1 minute pause between each interval followed by 5 minutes of recovery. Both protocols had the same T_R and the number of average of 2000 and 8, respectively, Figure 3.4. Data for the third subject was discarded because the subject explained after the scan they had previously ruptured their tendon. The two last subjects had almost the same protocol as the second subject (1 minute rest, three exercise intervals of 4 minutes with a 1 minute pause between each intervals and 6 minutes of recovery), with a larger number of averages, 32.

Figure 3.1 – *In vivo* spectroscopy.

3.1.3 Phosphorus MRS protocol

The spectroscopy measurements were performed on a 3 Tesla whole-body magnetic resonance scanner (Tim Trio; Siemens, Germany) using a single resonator surface coil that allows the receiving and transmit of ^{31}P resonances at 49.8719 MHz. A free induction of decay sequence, echo time of 0.35 milliseconds and a flip angle of 90 degree was used.

In this section the phosphorus spectrum of *in vivo* experiments confirms the accuracy and sensitivity of the coil frequency picking. Figure 3.1 shows the human calf muscle spectrum of ^{31}P spectroscopy on a control subject. Repetition time, echo time and number of the average are 2000 ms, 0.35 ms and 128, respectively. The sequence is

non-localized spectroscopy, that acquires the spectrum within 4 minutes and 16 seconds. The result is the real part of the spectrum after phase correction and it has been reported without any filter. Next, to observe the PCr variation during the exercise, we compared the PCr intensity while the subject was exercising and during recovery. Each trace in Figure 3.2 represents the spectra for each 2 minutes of acquisition. PCr -with the highest

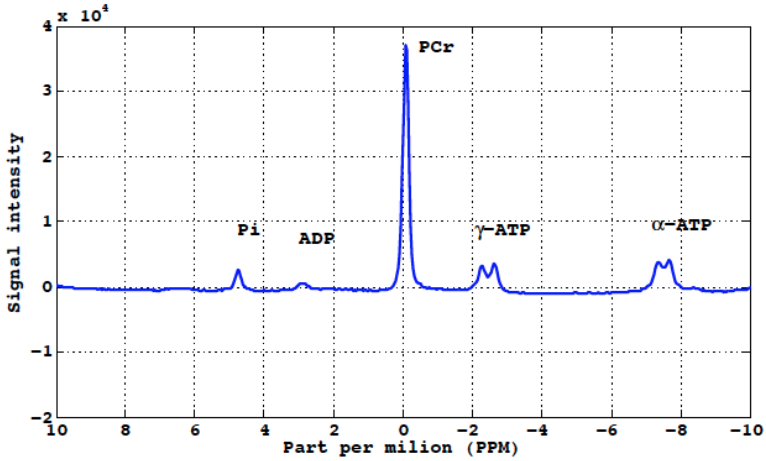

.png

Figure 3.2 – Spectrum of human calf muscle in resting state, 256 average, TR of 2000, fid sequence.

concentration among the other metabolite- is reduced during the exercise interval because it has to be degenerated to regenerate ATP to supply energy to the calf muscle. In this process PCr depletes exponential [43] such that, the highest decrease is within first 10-20 seconds after the exercise starts. During recovery, PCr gradually returns back to baseline values. According to the literature, the recovery part lasts 5 to 15 minutes [32], so to see complete PCr regeneration we corrected the protocol after the first subject. The recovery period was extended from four to six minutes. Also instead of 6 minutes of consecutive periods of exercise, they were broken into three 4-minute intervals with 1 minute of pause between each. Figure 3.3 shows the results. The black parts at the front of the figure represents the recovery part and shows PCr returning to baseline. The fast reduction of the PCr right after the exercise is also clearly seen in this image. We can see how PCr is changing during rest-exercise-recovery, while the other metabolites such as ATP and inorganic phosphate are hidden in represented spectrum as the number of the

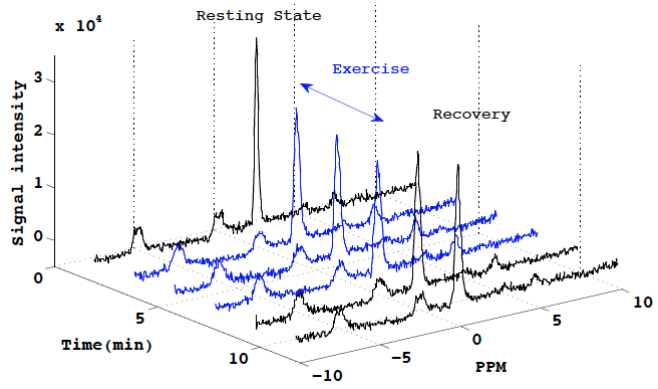

Figure 3.3 – First subject, exercise protocol: 2-minute resting period, 6 minutes of exercise and a 4-minute recovery period, T_R of 2000, 64 averages, fid sequence. Blue parts of the figure indicate the subject is exercising and the black parts belongs to resting and recovery periods.

average was quite low. However, we are interested in also observing their peaks. This is why the number of averages was increased to 32.

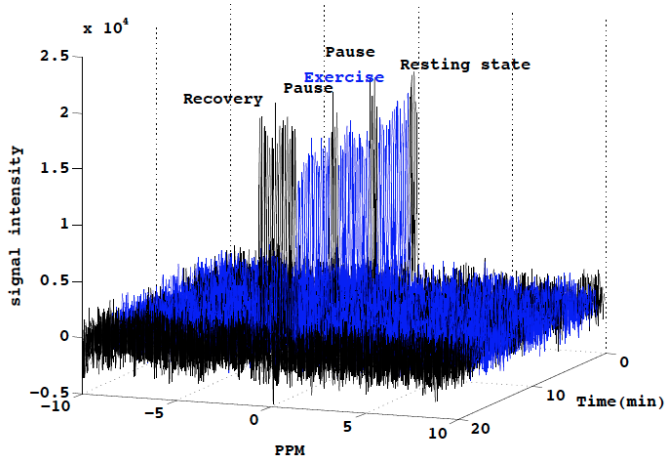

Figure 3.4 – Seconds subject, exercise protocol: 1 minute rest, three blocks of 4-minute exercise period followed by 1 minute pause and 6 minutes of recovery, 8 averages and T_R of 2000 using fid sequence

Figure 3.5 is the averaged spectra of subjects four and five. The patterns at -2.48, -7.52 and 5.02 ppm belong to γ-ATP, α-ATP and Pi, respectively. We see a small increase in Pi during the exercise phase since in all the muscle contraction ATP has to be

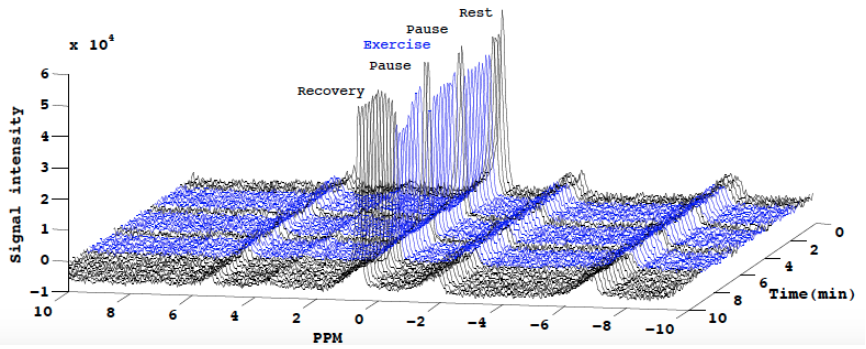

Figure 3.5 – Forth subject, exercise protocol: 1 minute of rest, 12 minutes of exercise and a 6-minute recovery period, 32 averages and T_R of 1000 using fid sequence.

breakdown and releases free energy. Muscles use this energy to contract by:

$$ATP \rightarrow ADP + Pi + energy \ : \ Muscle\ Contraction \tag{3.1}$$

3.2 Peak fitting in jMRUI

jMRUI is a JAVA-based user interface for analysis and processing of the NMR data and *in vivo* spectroscopy. To fit the peaks of the spectrum we used a quantitative method called advances method for accurate, robust, and efficient spectral fitting (AMARES). It involves prior knowledge including; spatial position of the resonance frequency of

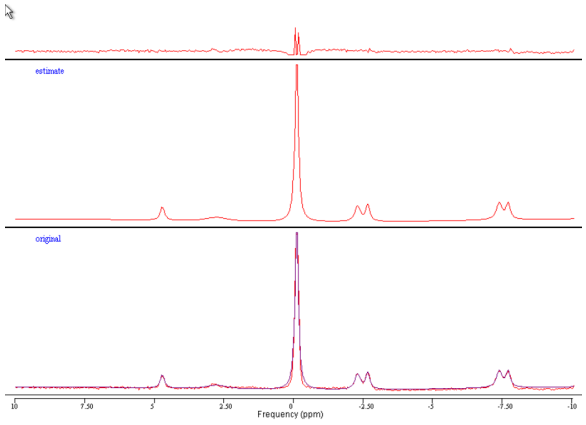

Figure 3.6 – Curve fitting of ^{31}P spectrum using AMARES and prior knowledge .

desired metabolites, desired line width of the peaks and the shape (Lorentzian or Gaus-

sian). With prior knowledge of the phosphorus spectrum in calf muscle AMARES fits the peaks of the spectrum. Figure 3.6 shows the peak fitting. The result is reported in three separate sections; the original data, the estimated spectrum based on the provided prior knowledge and the residual which has been removed from the estimate. The blue figure (estimated spectrum) overlaid the original spectrum.

CHAPTER 4

CONCLUSION AND FUTURE DIRECTION

4.1 Overview of work

Magnetic resonance spectroscopy is a non-invasive image modality that is an important diagnostic tool for the investigation the neuromuscular disorders. A highly natural abundance and the sensitivity of phosphorus provides a good quality spectrum within a relevant amount of time, in the scale of minutes. *In vivo* ^{31}P NMR provides the objective measurements of muscle energy metabolism during exercise and recovery. During exercise, a dynamic measurement of PCr using ^{31}P NMR spectroscopy within the human calf muscle can be measured. Given that the scanners supports proton metabolites and not working in multi-nuclear like ^{31}P, a home-made RF coil was required and tuned to desired metabolite frequency. An RF coil was developed to acquire the phosphorus spectrum. Experimental MRS data was obtained in a phantom as well as in human calf muscle to investigate the performance of the set-up. The results showed the main peaks of the phosphorus metabolite inside the phantom and the calf muscle with a appropriate resolution. The area under each peak of the metabolite is propertional to the number of present spins in the target area. The main phosphorus peaks in human calf muscle include: PCr, ATPs, ADP and Pi. We could reach adequate resolution in the acquired spectrum that not only the differentiation of the main consitituent of phosphorus metabolites is easy but even the j-coupling in ATPs is observable. Also a dynamic measurement of PCr – which is a highly concentrated metabolite within muscle – is reported. The depletion of PCr during the exercise was observed as a drop in its concentration, which based on the literature follows an exponential degradation. In the recovery state PCr intensity gradually returned back to the resting state.

4.2 Experimental setup

This project was started with the technical development of the hardware which in next step was used for clinical measurements. The main spectroscopy experiment involved plantar flexions exercises using a resistance band. To run the experiment the coil was placed under the calf muscle, two to four inch lower than the knee – Depending on the subject height – where the largest muscle of the lower leg is located. The participants asked to exercise for a period of 12 minutes, where the exhaustion is supposed to happen. Five subjects where involved in the *in vivo* experiments.

4.3 Existing defects and future works

The functional set-up offered promising results for this preliminary *in vivo* investigation. However, resistance is subjective as subjects were asked to hold the rubber band in their hand during the experiment. For different subjects we could not be sure the same resistance was being applied to their feet. On the other hand, subject motion during scanning could contribute to noise emerging in the spectrum as well as a drift in the spectrum. We used a single tuned RF coil with a small surface area, which is capable of imaging the area of muscle in closest proximity. As a next step, the RF coil could be re-designed to a larger surface coil operating in dual frequency, proton and phosphorus. A volume coil should also be fabricated in future to give access to deeper tissue penetration and larger coverage of the ROI as it is a crucial point in brain spectroscopy. During the experiment, some fid acquisitions were also acquired to find the optimum voltage that offers the highest signal intensity. In fact for the moment there is no direct way to optimize the transmitted voltage. In proton spectroscopy the voltage optimization could be done on-line using the provided plug-ins. To have these types of optimizations for phosphorus spectroscopy, sequence programming would be an important aspect to save time and unnecessary acquisition.

BIBLIOGRAPHY

[1] R. A. De Graaf. *In Vivo NMR Spectroscopy, 2nd Edition Principles and Techniques*. John Wiley and Sons,, 2007.

[2] H. J. A. int Zandt A. J. van den Bergh A. Heerschap, C. Houtman and B. Wieringa. Introduction to in vivo 31p magnetic resonance spectroscopy of (human) skeletal muscle. *Proceedings of the Nutrition Society*, 58:861–870, 1999.

[3] A. R. Barker and N. Armstrong. Insights into developmental muscle metabolism through the use of 31P-magnetic resonance spectroscopy: a review. *Pediatr Exerc Sci*, 22(3):350–368, Aug 2010.

[4] K. McCully, D. Mancini, and S. Levine. Nuclear magnetic resonance spectroscopy: its role in providing valuable insight into diverse clinical problems. *Chest*, 116(5):1434–1441, Nov 1999.

[5] L. Mosconi, V. Berti, L. Glodzik, A. Pupi, S. De Santi, and M. J. de Leon. Preclinical detection of Alzheimer's disease using FDG-PET, with or without amyloid imaging. *J. Alzheimers Dis.*, 20(3):843–854, 2010.

[6] I. J. Cox. Development and applications of in vivo clinical magnetic resonance spectroscopy. *Prog. Biophys. Mol. Biol.*, 65(1-2):45–81, 1996.

[7] P. Liu, M. S. Fleete, Y. Jing, N. D. Collie, M. A. Curtis, H. J. Waldvogel, R. L. Faull, W. C. Abraham, and H. Zhang. Altered arginine metabolism in Alzheimer's disease brains. *Neurobiol. Aging*, 35(9):1992–2003, Sep 2014.

[8] A. Greiner, R. Esterhammer, H. Messner, M. Biebl, H. Muhlthaler, G. Fraedrich, W. R. Jaschke, and M. F. Schocke. High-energy phosphate metabolism during incremental calf exercise in patients with unilaterally symptomatic peripheral arterial disease measured by phosphor 31 magnetic resonance spectroscopy. *J. Vasc. Surg.*, 43(5):978–986, May 2006.

[9] B. Wciso, M. Cichocka, and A. Urbanik. Phosphorus Spectroscopy of Calf Muscles before and after Exercise. *Pol J Radiol*, 79:328–332, 2014.

[10] J. W. Pettegrew, J. Moossy, G. Withers, D. McKeag, and K. Panchalingam. 31P nuclear magnetic resonance study of the brain in Alzheimer's disease. *J. Neuropathol. Exp. Neurol.*, 47(3):235–248, May 1988.

[11] W. R. Martin. MR spectroscopy in neurodegenerative disease. *Mol Imaging Biol*, 9(4):196–203, 2007.

[12] K. Kantarci. Proton MRS in mild cognitive impairment. *J Magn Reson Imaging*, 37(4):770–777, Apr 2013.

[13] J. Suzuki T. Toyooka, K. Nagayama and T. Sugimoto. Noninvasive assessment of cardiomyopathy development with simultaneous measurement of topical h-1 and p-31 magnetic resonance spectroscopy. *Circulation*, 86:295–301, 1992.

[14] P. A. Bottomely and R. G. Weiss. Non-invasive magnetic-resonance detection of creatine depletion in non-viable infarcted myocardium. *Lancet*, 351:714–718, 1998.

[15] D. B. Twieg A. A. Maudsley D. Sappeyarinier J. W. Hugg, G. B. Matson and M.W. Weiner. P-31 mr spectroscopic imaging (mrsi) of normal and pathological human brains. *Magnetic Resonance Imaging*, 10:227–243, 1992.

[16] W. Negendank. Studies of human tumors by mrs - a review. *NMR in Biomedicine*, 5:303–324, 1992.

[17] D. J. Griffiths. *Introduction to electrodynamics*. Prentice Hall, 1999.

[18] J. Kappenstein, A. Ferrauti, B. Runkel, J. Fernandez-Fernandez, K. Muller, and J. Zange. Changes in phosphocreatine concentration of skeletal muscle during high-intensity intermittent exercise in children and adults. *Eur. J. Appl. Physiol.*, 113(11):2769–2779, Nov 2013.

[19] THOMAS L. JAMES. *Fundamentals of NMR*. University of California, 1998.

[20] Neil E. Jacobsen. *NMR SPECTROSCOPY EXPLAINED*. John Wiley and Sons, Inc., 2007.

[21] Olaf Kuhl. *Phosphorus-31 NMR Spectroscopy: A Concise Introduction for the Synthetic Organic and Organometallic Chemist*. Springer Science and Business Media, 2008.

[22] Martha Bruch. *NMR Spectroscopy Techniques, Second Edition*. CRC Press, 1996.

[23] X. J. Zhou M. A. Bernstein, K. F. King. *Handbook of MRI Pulse Sequence*. Elsevier, 2004.

[24] T. L. Clanton, M. C. Hogan, and L. B. Gladden. Regulation of cellular gas exchange, oxygen sensing, and metabolic control. *Compr Physiol*, 3(3):1135–1190, Jul 2013.

[25] G. Walter, K. Vandenborne, K. K. McCully, and J. S. Leigh. Noninvasive measurement of phosphocreatine recovery kinetics in single human muscles. *Am. J. Physiol.*, 272(2 Pt 1):C525–534, Feb 1997.

[26] M. C. McCormick J. S. Baker and R. A. Robergs. Interaction among skeletal muscle metabolic energy systems during intense exercise. *Journal of Nutrition and Metabolism*, 19:904–926, 2010.

[27] A. Singh1 V. B. KC1 H. Hariharan1 M. Haris1, K. Cai1 and R. Reddy1. Chemical Exchange Saturation Transfer effect from Phospho-creatine (PCr) and Adenosine-tri-phosphate (ATP). ISMRM Conference, 2011.

[28] Douglas L. Rothman Robert G. Shulman. *Metabolism by In Vivo NMR*. John Wiley and Sons, 2005.

[29] G. J. Kemp, M. Meyerspeer, and E. Moser. Absolute quantification of phosphorus metabolite concentrations in human muscle in vivo by 31P MRS: a quantitative review. *NMR Biomed*, 20(6):555–565, Oct 2007.

[30] W. I. Jung, S. Widmaier, U. Seeger, M. Bunse, A. Staubert, L. Sieverding, K. Straubinger, F. van Erckelens, F. Schick, G. Dietze, and O. Lutz. Phosphorus J coupling constants of ATP in human myocardium and calf muscle. *J Magn Reson B*, 110(1):39–46, Jan 1996.

[31] K. K. McCully, E. Malucelli, and S. Iotti. Increase of free Mg2+ in the skeletal muscle of chronic fatigue syndrome patients. *Dyn Med*, 5:1, 2006.

[32] J. S. Baker, M. C. McCormick, and R. A. Robergs. Interaction among Skeletal Muscle Metabolic Energy Systems during Intense Exercise. *J Nutr Metab*, 2010:905612, 2010.

[33] J. S. Baker, M. C. McCormick, and R. A. Robergs. Interaction among Skeletal Muscle Metabolic Energy Systems during Intense Exercise. *J Nutr Metab*, 2010:905612, 2010.

[34] M. A. Drost C.C. Oomens G. J. Strijkers K. Nicolay J. J. Prompers, J. A. Jeneson. Dynamic mrs and mri of skeletal muscle function and biomechanics. *NMR Biomed*, 19:927–953, 2006.

[35] S. Nioka M. Kushmerick B. Chance, J. Im. Skeletal muscle energetics with pnmr: personal views and historic perspectives. *NMR Biomed*, 19:904–926, 2006.

[36] Eduard E. de Lange William E. Brant. *Essentials of Body MRI*. Oxford University Press, 2012.

[37] J. R. Griffiths J. T. Vaughan. *RF coils for MRI*. Wiley, 2012.

[38] Ananda Kumar. *Performance Optimization of Local Magnetic Resonance Surface Coils and Antennas*. ProQuest, 2009.

[39] L. Axel C. E. Hayes. Noise performance of surface coils for magnetic resonance imaging at 1.5 t. *Med Phys*, 12:604–607, 1985.

[40] Loren A. Zaremba. Guidance for industry and fda staff criteria for significant risk investigations of magnetic resonance diagnostic devices. Technical report, 2003.

[41] S. W. Provencher. *LCModel and LCMgui User Manual*. Wiley, 2011.

[42] G. Giovannetti, F. Frijia, L. Menichetti, M. Milanesi, J. H. Ardenkjaer-Larsen, D. De Marchi, V. Hartwig, V. Positano, L. Landini, M. Lombardi, and M. F. Santarelli. Hyperpolarized 13C MRS surface coil: design and signal-to-noise ratio estimation. *Med Phys*, 37(10):5361–5369, Oct 2010.

[43] M. Roussel, D. Bendahan, J.P. Mattei, Y. Le Fur, and P.J. Cozzone. 31p magnetic resonance spectroscopy study of phosphocreatine recovery kinetics in skeletal muscle: the issue of intersubject variability. *Biochimica et Biophysica Acta (BBA) - Bioenergetics*, 1457(1-2):18 – 26, 2000.